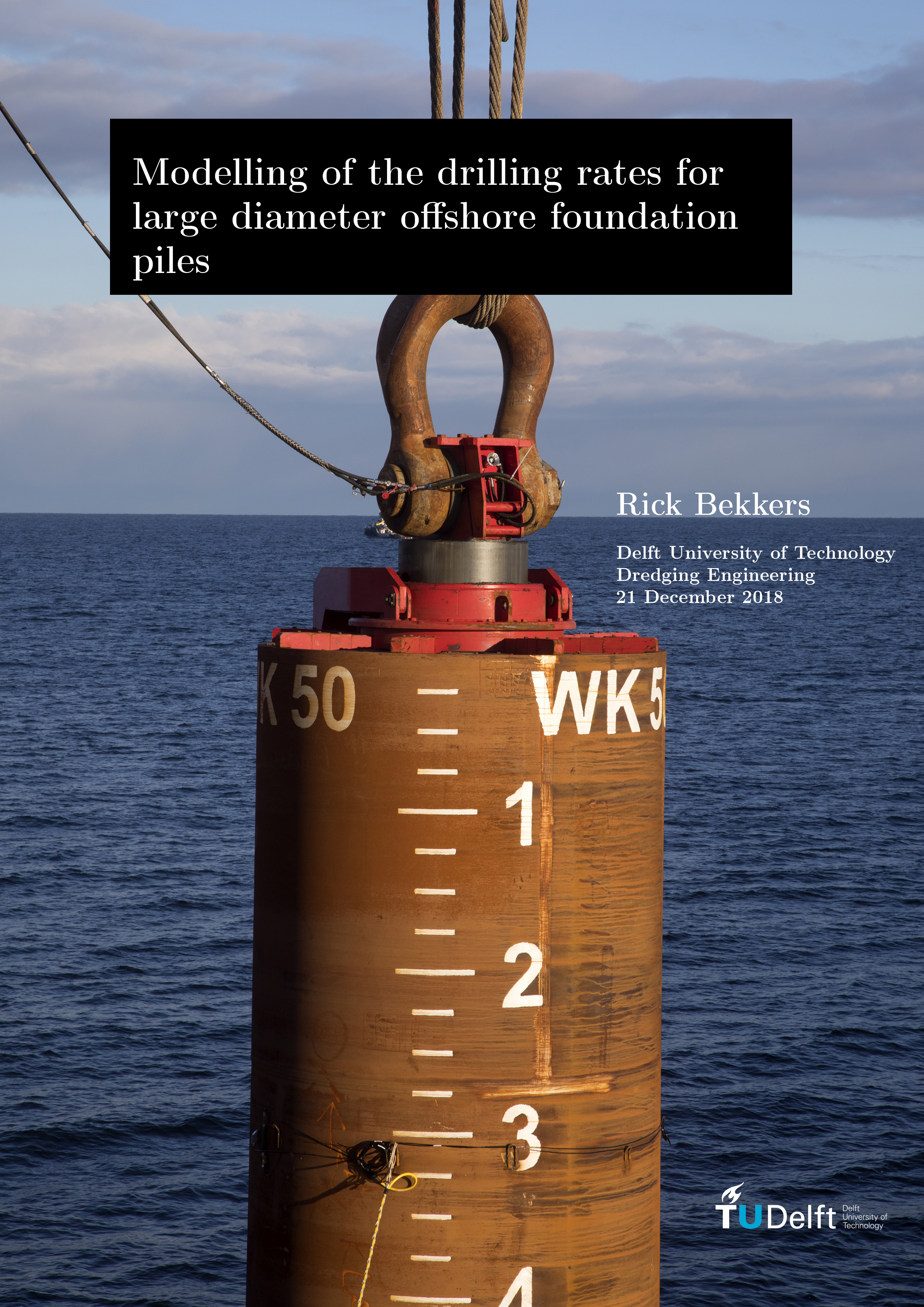

Modelling of the drilling rates for large diameter offshore foundation piles

Rick Bekkers

Delft University of Technology
Dredging Engineering

21 December 2018

Modelling of the drilling rates for large diameter offshore foundation piles

To obtain the degree of Master of Science in Offshore and Dredging Engineering

by

Rick Petrus Cornelis Bekkers

Dredging Engineering
Delft University of Technology

Version 1.0, December 21, 2018

Modelling of the drilling rates for large diameter offshore foundation piles

Author:
R.P.C. Bekkers

Thesis Committee:

Dr. ir. S.A. Miedema	TU Delft
Dr. ir. R.L.J. Helmons	TU Delft
Ir. I.K. van Giffen	Royal Boskalis Westminster N.V.
Dr. P.N.W. Verhoef	TU Delft

Acknowledgements

Voor u ligt mijn masterthesis ter afronding van de masteropleiding Offshore and Dredging Engineering aan de Technische Universiteit van Delft. Ik heb mijn thesis geschreven in opdracht voor Boskalis met als doel om meer inzicht te genereren in het proces dat plaatsvindt tijdens het boren van offshore fundatie palen. Gedurende mijn thesis heb ik een zeer fijne/leerzame tijd gekend en heb daarnaast veel leuke collega's ontmoet. Ik wil graag van deze gelegenheid gebruik maken om de personen te bedanken die hebben bijgedragen aan dit eindresultaat.

Veel dank gaat uit naar mijn begeleider Ike van Giffen vanuit Boskalis. Ik heb de samenwerking als zeer prettig ervaren en kon op elk moment bij je terecht. Je had altijd scherpe opmerkingen en was kritisch op mijn bevindingen, wat ervoor zorgde dat ik zelf ook kritisch bleef. Ook wil ik vanuit Boskalis graag specifiek Roeland Neelissen en alle collega's die mij hebben geholpen bedanken voor de betrokkenheid en het delen van kennis gedurende het project.

Vanuit de TU Delft wil ik graag mijn begeleider Rudy Helmons en Sape Miedema bedanken. Rudy, bedankt voor de persoonlijke begeleiding, leuke discussies en positieve commentaar. Na elke meeting had ik gevoel weer een stapje dichter bij het einddoel te zijn. Ook Sape bedankt voor het advies en begeleiding tijdens de meetings. Voorafgaand aan de thesis zijn we elkaar al meerdere keren tegen gekomen op de opleiding. Ik heb uw lessen en advies altijd als waardevol ervaren, welke ik zal meenemen gedurende de rest van mijn carrière.

Tot slot wil ik graag mijn familie en vrienden bedanken. Jullie hebben mij altijd gesteund tijdens mijn opleiding en in de keuzes die ik maak. Daarnaast voel ik me gezegend dat allebei mijn grootouders dit nog in goede gezondheid mee kunnen maken. Jullie laten mij zien wat de belangrijke dingen in het leven zijn en hoop ooit later in dezelfde positie te kunnen staan.

Rick Petrus Cornelis Bekkers 21 December 2018

Abstract

In a world where the awareness of global warming and climate change increases, the shift towards sustainable energy is essential. In the upcoming years, an increasing number of offshore wind farms is expected. Over the past years, all the 'best spots' are taken and the new locations in tougher soil conditions or even rock have to be overcome. The conventional pile driving technique is a less attractive solution here, because there is a significant chance to pile buckling. Drilling is an alternative method which is able to complete these installations successful in tougher soils and rock. Furthermore, in certain regions, the rules with respect to maximum noise levels during pile driving become stricter these days and the use of noise mitigation measurements can significantly increase the costs of the installation. Drilling can be an alternative method which decreases the noise generated during the installation.

The drilling phase plays a crucial role in the total drilling process, which can easily take up more than half of the total pile installation time. For installing a large amount of foundation piles, it is important, especially during the tender phase of a project, to have a good prediction of the drilling rate. Currently, the available drilling rate models are mainly empirical and therefore tend to be specific to a certain drilling method in a particular type of rock. The goal of this thesis is to give a better prediction of the drilling rate, which is applicable for various amount of large diameter drills. In order to predict the drilling rate, a theoretical based model is developed. The model consists of an excavation and a transportation part, which can both limit the drilling rate.

The excavation model determines the excavation limit of the drill. It makes a distinction between cutter heads that consist of pick points and cutter heads that consist of rollers cutters, which can be further distinguished into tooth, button or v-shaped discs cutters. In order to calculate the drilling rate, a literature study is done towards the excavation process of rock, where the existing cutting and indentation models are reviewed and incorporated within the model.

The transport model determines the transportation limit of the drill. The rock chips, generated by the excavation process, need to be transported in order to continue the drilling process. In most cases, transportation of cuttings takes place by the use of an airlift system. To model the limit of an airlift system, the momentum balance over the length of the airlift pipe is solved, which defines the maximum quantity of solids that is able to be transported.

The model shows a good resemblance with experimental results obtained from the raise boring industry. Furthermore, a similar trend is observed between the model and values obtained from offshore drilling manufacturers. It is now possible to give a theoretical based prediction of the drilling rate for the installation of drilled foundation piles, which is applicable for a wide range of large diameter drills.

Contents

Nomenclature

Greek

Symbol	Description	Units
α	Half tip angle	[°]
α_x	Vapour quality ratio	[-]
β	Rake angle	[°]
δ	External friction angle	[°]
δ_{li}	Crack length	[m]
ϵ	Mean relative deviation	[%]
ϵ_a	Deviation	[%]
ϵ_w	Wall roughness	[mm]
γ	Clearance angle	[°]
γ_{li}	Rock surface energy density	[J/m^2]
λ	Friction factor	[-]
λ_{li}	Cutting force coefficient	[-]
ν	Kinematic viscosity	[m^2/s]
ω	Shear angle	[°]
ω_r	Rotational speed	[rpm]
ϕ	Angle of attack	[°]
ψ	Break out angle	[°]
ρ	Density	[kg/m^2]
σ	Stress	[Pa]
σ_n	Normal stress	[Pa]
σ_n	Unconfined Compressive Strength	[Pa]
σ_s	Critical stress	[Pa]
$\sigma_s t$	Stamp strength	[Pa]
σ_t	Brazilian Tensile Strength	[Pa]
τ	Shear strength	[Pa]
θ	Angle with cutting direction	[°]
φ	Internal friction angle	[°]
ξ	Friction coefficient	[-]
ζ_f	Particle shape factor	[-]

xi	Friction loss coefficient	[-]

Roman

Symbol	Description	Units
A	Area	[m^2]
B	Constant	[-]
b	indenter radius	[m]
C	Concentration	[-]
c	Cohesive shear strength	[Pa]
C_d	Drag coefficient	[-]
c_m	Mobilized cohesive shear strength	[Pa]
D	Diameter	[m]
d	Cutting depth	[m]
E	Young's modules	[Pa]
f	Friction factor	[-]
F_N	Normal force	[Pa]
F_T	Tangential force	[Pa]
G	Momentum	[Ns]
g	Gravity	[m/s^2]
j	Flux	[m/s]
K	Temperature	[K]
K_{Ic}	Fracture toughness	[Pa $\sqrt{m}$]
L	Length	[m]
l	Distance	[m]
m	Ductility number	[-]
MCF	Mean cutting force	[N]
MNF	Mean normal force	[N]
N	Number of experiments	[-]
n	Stress distribution factor	[-]
n_h	Hindered settling particle factor	[-]
nr	Number	[-]
P	Thrust	[N]
p	Pressure	[Pa]
PCF	Peak cutting force	[N]

PNF	Peak normal force	[N]
Q	Production	[m^3]
q	Dynamic pressure loss	[Pa]
R	Gas constant	[J/kg K]
r	Radius	[m]
r_c	Correlation coefficient	[-]
Re_p	Particle Reynolds number	[-]
s	Spacing	[m]
T	Torque	[Nm]
V	Volume	[m^3]
v	Velocity	[m/s]
w	Width	[m]
w_0	Settling velocity	[m/s]
w_S	Hindered settling velocity	[m/s]
X	Dimensional correction factor	[m]
z	Water depth	[m]
q	Dynamic pressure loss	[Pa]

Abbreviation	**Description**
BTS	Brazilian Tensile Strength
ROP	Rate Of Penetration
RQD	Rock Quality Designation
SEL	Sound Exposure Level
TCI	Tungsten Carbide Insert
UCS	Unconfined Compressive Strength

List of Figures

List of Tables

1 Introduction

1.1 Development of drilling in the offshore wind industry

The offshore wind industry is a fast growing market. In 2017, Europe has a cumulative installed capacity of more than 16 GW with more than 3 GW installed that year. Figure 1.1 shows the installed capacity per year (WindEurope, 2017). In the upcoming years, an increasing number of offshore wind farm installations is expected. The foundations are preferably installed in relative limited water depth and soil that allows for pile driving. Unfortunately, these conditions are not always present. With the increasing amount of wind farms, the 'best spots' are taken and the new locations will be in deeper waters or in tougher soil conditions. For example, along the European coasts large chalk formations exist as shown in Figure 1.2, where installing piles using the pile driving method is not an option. The driveability of piles is often determined by the Unconfined Compressive Strength (UCS) value. Pile drilling can be a solution for these areas which exceeds their limit. According to Stevens et al. (1982), this limit is at an UCS value of approximately 5 MPa. The foundations in rock are in most cases equipped with three or four legs. These tripods or jacket structures use thinner and shorter piles, which are easier to handle in harder soils compared to the standard large diameter monopiles.

When the chance of refusal during pile driving is relatively small, which means that the driveability of foundation piles is high, it is beneficial to drive the piles to the moment they exceed their driving limit. To drive the pile any further, excavation of the material inside and underneath the pile is required using a large diameter drill. Afterwards, the pile can reach sufficient depth by regular pile driving. This method of installation is called the drive-drill-drive method.

Another method of installing offshore piles is the drill and grouted method, which can be a solution when the driveability is not sufficient and the chance of pile refusal is relatively high. The holes are drilled before the installation of the piles and grouted afterwards. This technique ensures an installation without bringing any damage to the piles and takes away the chance of pile buckling.

Drilling foundation piles will become more interesting in the future and can also be an option when the driveability is sufficient. Drilled and grouted piles are shorter in length due to the grouted connection which increases the lateral capacity of the pile. Subsequently, the rules with respect to maximum noise levels during pile driving become stricter and the use of noise mitigation measurements increase the costs of the installation. According to the German Federal government, the sound exposure levels (SEL) have been set to 160 dB and 190 dB for peak pressure levels at 750 meters distance from the pile. During drilling, the expected noise exposures are 117 dB and 122 dB for peak pressures at a distance of 750 m (Koschinski and Lüdemann, 2013).

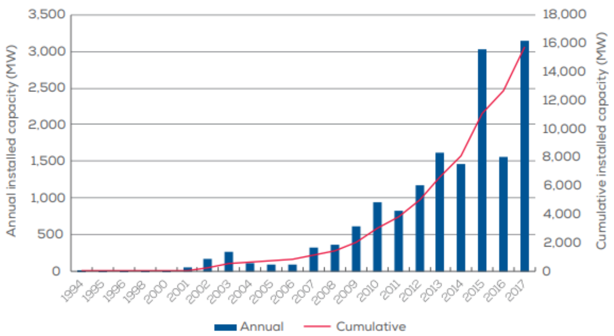

Figure 1.1: Growing market offshore wind industry (WindEurope (2017)).

Figure 1.2: Geological map of France (modified from Geo).

1.2 Problem definition

The number of offshore foundation piles that require drilling increases in the upcoming years. In the offshore industry, several drilling and installation methods are available, that can be operated from a floating vessel or jack-up. The choice for a specific method is project dependent and it is therefore hard to select one standard drilling method for all operations. In order to determine the right combination of the drilling tool and operating vessel, it is important to know the total drilling time, which can easily take up half of the total installation time.

Currently, the method for estimating the drilling rate is mainly empirical and far less-well understood for different types of rock. Nowadays subcontractors give an estimation of the drilling rate in the order of several meters per hour. The operation can require more than 40 hours, but it can also be finished within 10 hours when the rock characteristics are favourable. As a result, this can have a large influence on the expected installation time when multiple piles have to be drilled. To understand which parameters limit the drilling rate, more insight in the excavating and transportation process is required to give a better prediction of the drilling rate during the tender phase of the project. To obtain this goal, the focus of this thesis is on the drilling process of large diameter drills and the following research objective was set:

Develop a theoretical based model that predicts the drilling rate for the installation of offshore foundation piles which is applicable for different drilling techniques.

In order to fulfil the main research objective, the following steps are defined:

1. Analyse the different type of drilling and transport techniques that exist in the offshore drilling industry.
2. Explain the physical phenomena of rock excavation using different tools.
3. Determine the dominant parameters that influence the drilling rate.
4. Describe the existing theoretical models to calculate the forces on the excavation tools.
5. Execute a literature study to the working mechanism of the transport system.
6. Design a drilling model that predicts the rate of penetration which consist of an excavation model and a transport model.
7. Validate the model using drilling data.

1.3 Outline of this thesis

The report contains of six chapters. In Chapter 2 a broad introduction to the main offshore drilling and transport techniques is presented. Chapter 3 consist of three parts. The first part discusses the rock characteristics and the main parameters that influence the drilling rate. The second part gives an overview of the existing (semi-)theoretical and empirical linear rock cutting models and the third part discusses the indentation models for a single indenter and the application to roller bits. In Chapter 4 the drilling model is presented that predicts the rate of penetration and in Chapter 5 the validation of the model, by comparing it to experimental data, is given. Finally, Chapter 6 concludes the report according to the objective and gives recommendations for further research.

2 | Drilling and transport techniques

This chapter provides a literature review of the drilling and transport techniques used in the offshore industry. The first part describes the main drilling techniques, after which several alternative techniques will be elaborated in the second part. The third part makes a distinction between the different excavation techniques that are used to excavate the rock. Finally, the transport methods are discussed and more insight in the working principle of an airlift system is given.

2.1 Main drilling techniques

2.1.1 Pile-Top drill

The majority of offshore drills are Pile-Top drilling rigs, as shown in Figure 2.1. The drill rig operates from a platform which is installed on top of a pile where all the machinery is placed. The drill is guided downwards through the pile until it reaches the seabed. The drill head contains several amount of roller bits which excavate the rock by indenting. A reverse circulation drilling (RCD) technique transport the rock chips upwards through the inside of a drill string by the use of an airlift system. This is reversed compared to the standard circulation drilling technique, where normally fluid is pumped downwards through the drill string and the chips are removed upwards at the outside of this string.

2.1.2 Subsea drill

Nowadays the offshore wind industry shifts towards deeper waters and the market asks for shorter installation times. A solution for this is to use a completely submerged drill rig. The subsea drill uses the same technique as the Pile-Top Rig, but does not have a drill string mounted towards a platform (Figure 2.2). This leads to a decrease in installation time before drilling. During the operation, a conductor casing is placed inside a template that is fixed to the seabed. Additionally, the drill rig, which consists of a rotary drive, drill pipe, heavyweights and a drill head, is lowered into the conductor casing. During the drilling phase, chips are transported with the RCD technique and released shortly above the drill. Besides shorter installation time, the drill rig is also able to work under higher environmental loads. However, operating subsea leads to more submerged mechanical components which make the drill more vulnerable.

Figure 2.1: Pile-top Drilling Rig (DTH).

Figure 2.2: Subsea RCD drill BSD3000 (Bauer, 2016a).

2.2 Alternative drilling techniques

Companies are still looking for faster, cheaper and simpler methods to excavate the rock for installing offshore foundation piles. This section describes the upcoming alternative drilling techniques in the industry.

2.2.1 Dive drill

A drilling technique that support the drive-drill-drive method is for example the Dive Drill from Bauer (2016a). It is a rotary drilling system which clamps itself to the inner wall of the foundation pile. Torque is generated in the rotary drive and transmitted to the drill head with a telescoping drill string. A big difference of the Dive Drill, compared to standard drill rigs, is that it uses another failure mechanism to excavate the rock. Instead of indentation, the drill uses a cutting technique that consist of multiple pick points.

During drilling, chips are fed to a cone crusher, mixed with seawater and pumped with a centrifugal pump to the surface or can be deposited in the water. The Dive Drill is able to work 1.5 meters below the pile tip. To continue the drilling process, the pile first needs to be driven further for the clamping system to work.

A big advantage of the Dive Drill with respect to the Top-Drill is that it has a higher drilling rate. Furthermore, with a top drill extra time is required to add and remove rods during the drilling operation. A disadvantage of the Dive Drill is that it has to operate alternating with a driving hammer, because it can only work up to 1.5 meters below the pile tip.

2.2.2 Drilling bucket

Using a drilling bucket is well known onshore and is nowadays also used in the offshore environment. It works with a rotary drilling unit, kelly bar and hoist rope connected to the base carrier crane (Figure 2.3). An example of a drilling bucket is the so called Fly Drill from Bauer (2016a). The drill is attached to a crane on the vessel and uses hydraulic power to rotate. During the operation, the drill clamps itself to the top of a pile that needs to be installed. The drill is lowered by a kelly bar up to the moment it reaches the seabed. After drilling a certain depth, the bucket needs to be emptied outside the pile. This gives the opportunity to swing the bucket sideways and collect the material when it is not allowed to deposit the material in the water.

Figure 2.3: Flydrill (Bauer, 2016a).

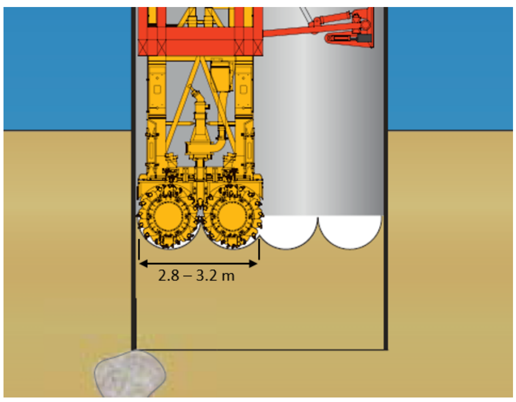

Figure 2.4: Trench cutter (Bauer, 2016a).

2.2.3 Trench cutter

A trench cutter is a drilling technique equipped with two cutter wheels which rotate in opposite direction. The cutter head is able to cut into any type of soil and rock (Bauer (2016a)). The cutter length varies between 2.8 and 3.2 m and is therefore used in the offshore environment for the installation of monopiles (Figure 2.4). This thesis focuses mainly to the installation of foundation piles for jacket or tripod structures and is therefore not covered any further in this report.

2.3 Excavation mechanisms

In order to predict the drilling rate, the excavation process plays an important role. Every drill uses a certain amount of torque, thrust and rotational speed to excavate a layer of rock. Looking at only the drill head, basically two different excavation types can be distinguished:

- Cutting type
- Indentation type

Both types will be described further in de following section.

2.3.1 Cutting type

Cutting tools excavate the rock by making a horizontal movement through the rock surface. They can be separated into chisel shaped tools and conical pick points. Figure 2.5 shows a drilling bucket with chisels mounted to the drill head. They are recommended for soft, non-abrasive rocks. For more tougher rocks, pick points are often used (Figure 2.6). They are able to excavate rocks which have an Unconfined Compression Strength (UCS) value up to around 100 MPa as shown in Figure 2.7 and are therefore very interesting for drilling rock.

Figure 2.5: Drilling bucket with chisel shaped tools (STD).

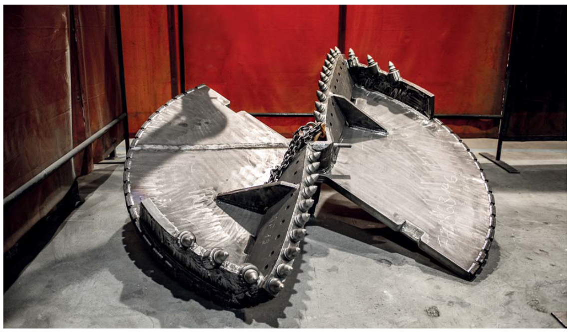

Figure 2.6: Drill head with pick points (Bauer, 2016b).

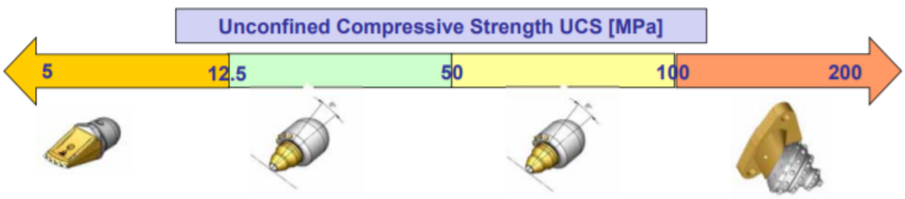

Figure 2.7: Suitability of cutting tools per UCS (GmbH, 2012).

2.3.2 Indentation type

The majority of the large diameter offshore drills are Pile-Top Rigs, which use an indentation mechanism to excavate the rock. The drill head consists of multiple roller bits as shown in Figure 2.8. With the right amount of thrust and torque, bits indent the rock. This leads to cracks that propagate through the rock. Small chips are generated and removed with the RCD technique through a suction hole which is shown in Figure 2.9. The roller bits can be separated into three different types; tooth cutters, button cutters and v-shaped disc cutters (MHWirth, 2016).

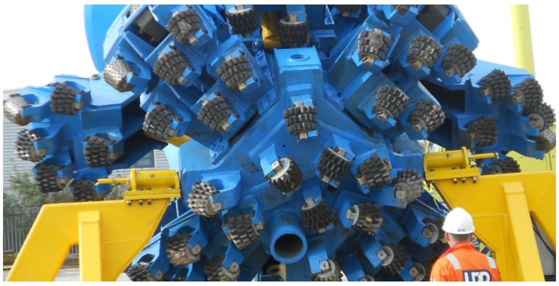

Figure 2.8: Large diameter drill head with roller bits. (LDD5000)(LDD).

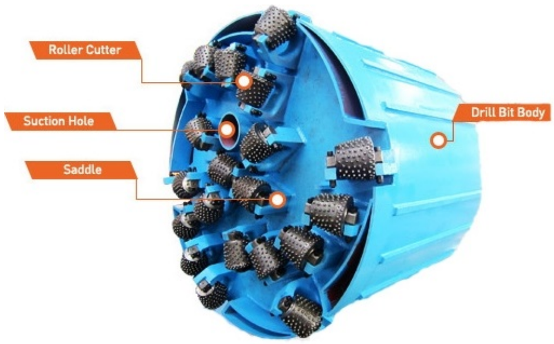

Figure 2.9: Configuration of a large diameter drill head.(LTD, 2015).

Tooth cutters
Tooth bits (Figure 2.10a) are designed for drilling soil and rock layers such as siltstone, chalk and shales with UCS values between 0 and 75 MPa and can resist a load of 40 kN each. Due to their long and sharp teeth, the rollers not only indent the material, but also have a scraping action.

Button cutters
Button bits (Figure 2.10b), also called Tungsten Carbide Insert (TCI) bits are designed for drilling hard rock layers with UCS values between 70 and 250 MPa. The rollers are made of steel inserted with tungsten carbide buttons, can have a load up to 140 kN each, have a high wear resistance and a long lifetime. During excavating, bits indent the rock which leads to the formation of cracks. When they propagate, little chips break out of the rock formation.

V-shaped studded disc cutters
V-shaped studded disc cutters (Figure 2.10c) are designed for drilling very hard rock layers with an UCS value between 80 and 350 MPa. The rollers can resist a load of 140 kN and creates grooves in the rock while rolling over the surface. Every groove leads to the formation of cracks which ensures the break out of chips between the grooves.

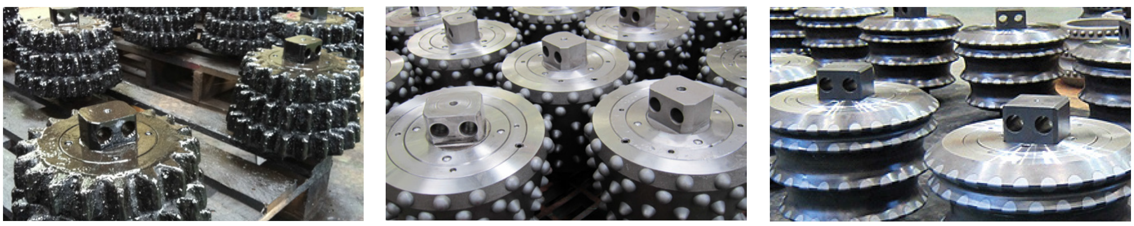

(a) Tooth cutter. (b) Button cutters. (c) V-shaped studded disc cutters.

Figure 2.10: Different roller bit configurations according to LTD (2015).

2.4 Transport methods

While drilling a large diameter hole, not only the excavation process can limit the drill speed, but also the transportation process of the excavated material plays a crucial role during drilling. Rock chips are generated underneath the drill head and needs to be transported to continue the drilling process. This can be succeeded in several ways. The most common technique is by an airlift system. The method has been known since the late 18th century and is namely used for transporting water, aggressive fluids and solids. A big advantage of the airlift compared with other methods is that the technique is simple and does not require a lot of space, there are rarely breakdowns and doing maintenance is simple.

The airlift system consists of a pipe from the drill head to the top of the drill (riser tube). A compressor above the water surface injects air through a tube in the injection point just above the drill head. As the air rises and expands within the drill string, the fluid density inside the pipe reduces. This leads to an upward flow in the pipe which transports the chips underneath the drill head as is shown in Figure 2.11.

Other options, but less common, are the centrifugal pump and the drilling bucket. Often the transport limit of these techniques is already known and therefore not further analyzed within this report.

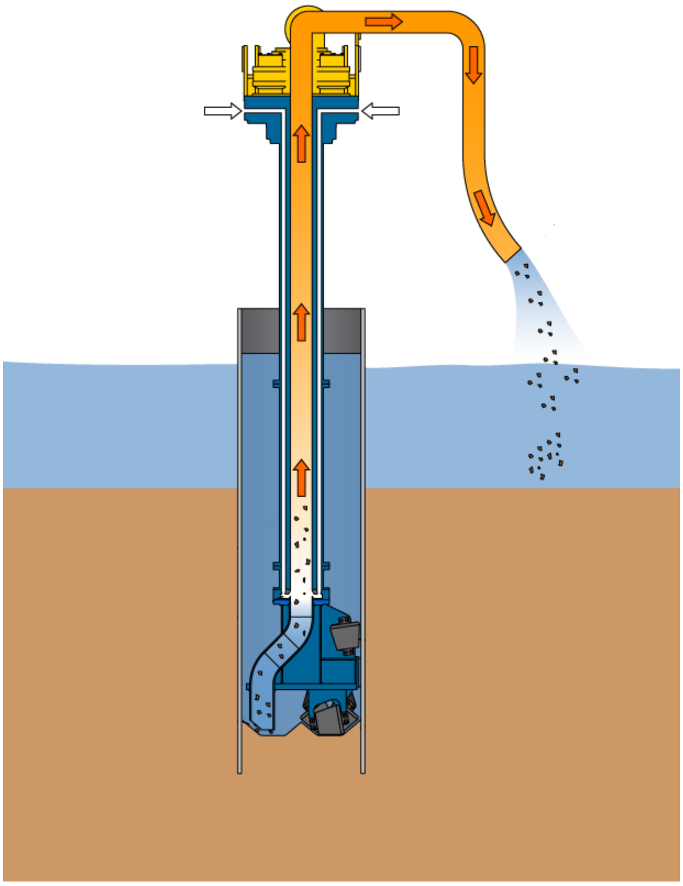

Figure 2.11: Reverse circulation drilling technique (modified from Seacore (2014)).

3 | Rock excavation theory

This chapter consists of three parts. The first part discusses the rock characteristics and the main parameters that influence the drilling rate. The second part gives a broad overview of the existing (semi-)theoretical and empirical linear rock cutting models. The third part discusses the indentation models for a single indenter and the application of roller bits.

3.1 Rock characteristics

The choice for a certain excavation mechanism and corresponding drilling rate depends a lot on the type of rock. There are basically three different types of rocks to distinguish; igneous, sedimentary and metamorphic rocks. Igneous rocks form due to the cooling of magma deep inside the earth, metamorphic rocks are formed by the change of igneous and sedimentary rocks and sedimentary rocks due to the solidification of sediment.

Sedimentary rock is present in most cases of drilling and dredging applications. These rocks can be ordered from extremely weak to extremely strong with a classification system based on the Unconfined Compressive Strength value (Table 3.1). Drilling foundation piles for the Offshore Wind industry normally takes place in weak to strong rocks (R0 & R1 & R2 & R3), with varying UCS values from 1 to 100 MPa. The depth profile is rarely homogeneous and often the top layer consists of an overburden soil layer. Different layers can be present such as sand or clay, but also strong rock layers could exist, and the presence of boulders influence the drilling rate.

Two parameters that are often linked to the drilling rate are the Unconfined Compressive Strength (UCS) and the Brazilian Tensile Strength (BTS). The UCS value indicates the shear strength of the material, while the BTS value determines the tensile strength.

Table 3.1: Rock classification on the basis of Unconfined Compressive Strength (Gokhale, 2010).

Class	*Uniaxial compressive strength in MPa*	*Point load index in MPa*	*Schmidt hardness by L – hammer*	*Method of strength in the field*	*Examples of rocks in the class*
R5 – Extremely Strong	>250	>10	50–60	Rock material only chipped under repeated hammer blows	Fresh Basalt, Chert, Diabase, Gneiss, Granite, Quartzite
R4 – Very Strong	100–250	4–10	40–50	Requires many blows of a geological hammer to break intact rock specimens	Amphibolite, Sandstone, Basalt, Gabbro, Gneiss, Granodiorite
R3 – Strong	50–100	2–4	30–40	Hand held specimens broken by a single blow of a geological hammer	Limestone, Marble, Phyllite, Sandstone, Schist, Shale
R2 – Medium Strong	25–50	1–2	15–30	Firm blow with geological pick indents rock to 5 mm, knife just scrapes surface	Claystone, Coal, Concrete, Schist, Shale, Siltstone
R1 – Weak	5–25	–	<15	Knife cuts material but too hard to shape into triaxial specimens	Chalk, Rocksalt, Potash
R0 – Very Weak	1–5	–	–	Material crumbles under firm blows of geological pick, can be scraped with knife	Highly Weathered or Altered Rock
Extremely Weak	0.25–1	–	–	Indented by thumbnail	Clay Gouge

Another parameter that influences the drilling rate is the fracture spacing in rock. Often the Rock Quality Designation (RQD) is linked to this parameter as a percentage, which equals the summation of the length of the pieces that are longer than 10 cm from a borehole core divided by the total length of the core. A low RQD value indicates a large number of fractures which refers to weathered rock. If the RQD value is high, the borehole core is mainly intact and refers to fresh rock. With a low RQD value the amount of fractures is relatively large which increases the drilling rate. However, the excavation depth of a drill is often in the order of a few mm per revolution, which makes it hard to couple the influence of RQD value directly to the drilling rate.

Other parameters that can influence the drilling rate are the porosity, density, permeability, abrasiveness, toughness and the Young's Modulus of the rock. Often these parameters are uncertain during the tender stage of the project and the influence on the drilling rate is unknown. Pore fluid effects of saturated rock are not incorporated within this research, while publicly available literature is limited and no direct relationship with the existing atmospheric rock cutting models is found.

The effect of water depth is assumed to be limited. Drilling foundation piles normally takes place in water depths up to 100 m. The maximum pressure differences that can occur in the cracks in these depths is in the order of 0 to 1 MPa. According to Vlasblom (2007), the influence of the water depth on the crack propagation in rock layers with a BTS value in the order of 5 MPa is limited. However, cutting very weak rock, with a BTS value in the same order as the water pressure difference, the water depth can affect the cutting forces.

Helmons et al. (2016a) modelled the effect of water depth on the rock cutting process with the use of a Discrete Element Method for rock. A comparison between the simulations and the results of the hyperbaric rock cutting experiments of Grima et al. (2015) is shown in Figure 3.1. In general, the cutting forces increase as the hyperbaric pressure increases. Under high hyperbaric conditions, the brittle failure behaviour of rock tends to become more ductile. Helmons et al. (2016a) simulated the experiments with a chisel, that cuts a layer of 0.02 m, with a velocity of 1 m/s in rock with an UCS value of approximately 9 MPa and a BTS value between 1 and 1.5 MPa for varying ambient pressures in dry conditions. No significantly increase in cutting force is found till a value of 1.5 MPa. However, still an increase in cutting force of approximately 30% is visible.

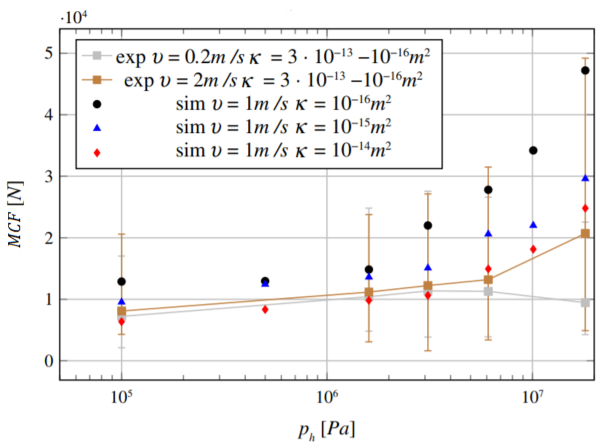

Figure 3.1: Comparison between experiments of Grima et al. (2015) and simulations of Helmons et al. (2016a). Plot shows averaged cutting force with respect to hydrostatic pressure. The error bars of the experiments correspond with the minimum and maximum measured cutting forces.

3.2 Rock cutting theory

3.2.1 Physical phenomena of rock cutting

Cutting of rock can be based on ductile or brittle failure. Figure 3.2 shows the cutting force of these two failure modes over time (Verhoef, 1997). Ductile failure has more or less a constant cutting force, while brittle failure shows a more saw-toothed behaviour of the force corresponding to the chip formation process. To distinguish if a rock fails in brittle or in ductile mode, researchers often use the ductility number m:

$$m = \frac{\sigma_c}{\sigma_t} \tag{3.1}$$

Where σ_c is the Unconfined Compressive Strength and σ_t is the Brazilian Tensile Strength. The m factor can be divided into a brittle and a ductile regime. When $m < 9$ ductile failure occurs and when $m > 15$ brittle failure occurs. When m is between 9 and 15 the failure mode is in a transition area which is called the brittle / ductile regime.

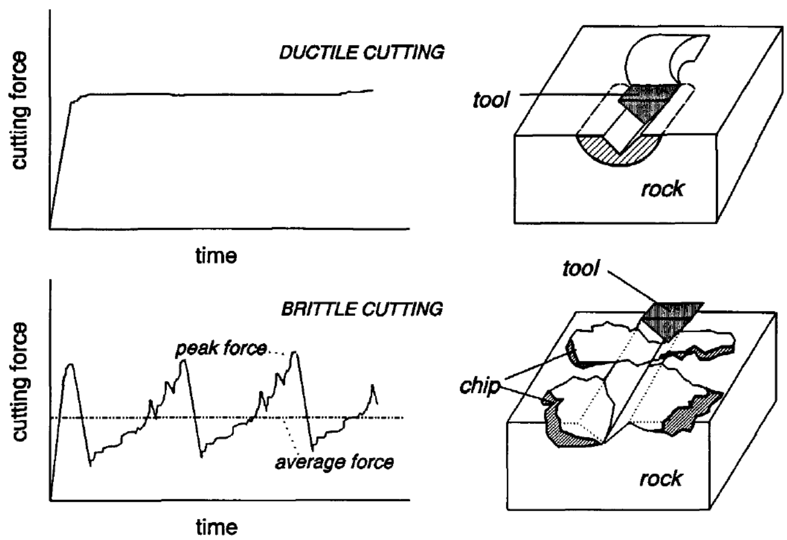

Figure 3.2: Ductile and brittle rock cutting according to Verhoef (1997).

During the excavation of brittle rock, a crushed zone occurs in front of the pick. When a pick point reaches sufficient depth, cracks are formed at the boundary of this zone. Just outside this zone, the crack can propagate towards the surface and generates a chip (Figure 3.3). This phenomena is often referred to as brittle failure. When a pick point does not reach the sufficient depth, it is not able to generate chips. It scratches over the rock surface and creates a crushed zone along the whole depth which is referred to as ductile failure (Figure 3.4).

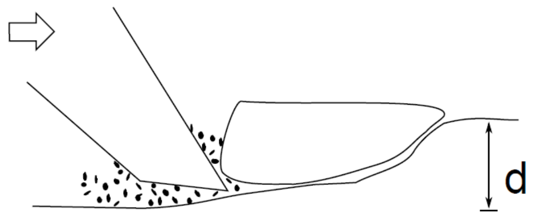

Figure 3.3: Brittle cutting process with large cutting depth (Helmons et al., 2016b).

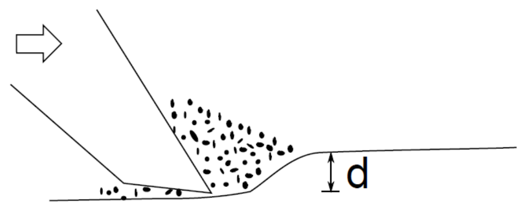

Figure 3.4: Ductile cutting process with small cutting depth. (Helmons et al., 2016b).

Richard et al. (1998) suggest that the critical depth where the ductile failure transfers into brittle failure scales with:

$$d_{crit} \propto (\frac{K_{Ic}}{\sigma_c})^2 \tag{3.2}$$

Where d_{crit} is the critical cutting depth and K_{Ic} is the fracture toughness of the rock.

Also, a difference in cutting force is noticeable between the brittle and ductile failure modes as is shown in Figure 3.5. According to Richard et al. (1998), two different relations can be distinguished. For ductile failure the mean cutting forces scale according to:

$$\frac{MCF}{w} \propto \sigma_c d \tag{3.3}$$

Where w is the width of the tool and d is the cutting depth. In the brittle regime, the formation of cracks dominates the process. Therefore, the mean cutting forces scale with the fracture toughness K_{Ic} according to:

$$\frac{MCF}{w} \propto K_{Ic}\sqrt{d} \tag{3.4}$$

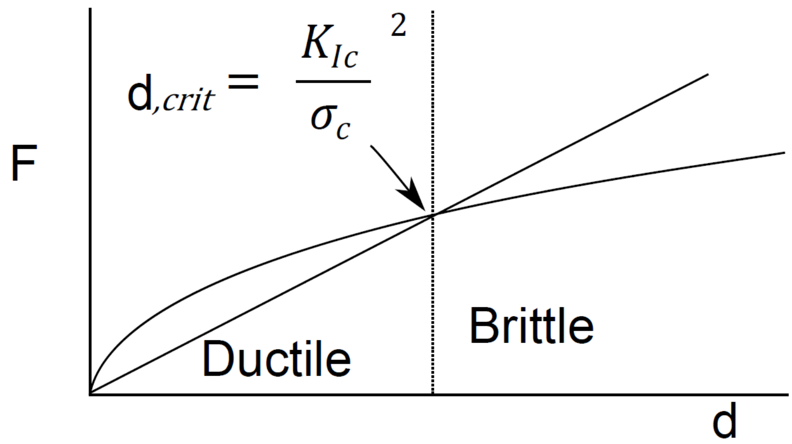

Figure 3.5: Scaling of the cutting force with respect to the cutting depth according to Richard et al. (1998) (modified from Helmons (2017)).

3.2.2 Theoretical & semi-empirical rock cutting models

This section describes the theoretical models of Nishimatsu (1972) Evans (1964), Miedema (2014), Evans (1984), Goktan (1997), Goktan et al. (2005) and Li et al. (2018). Some of them are theoretical, where others are modified to semi-empirical formulas. They all calculate the peak cutting forces in brittle rock, where the failure process can be either tensile or shear dominated.

The theoretical models often use different symbols for the same parameter. Therefore, the models are modified towards one frame of reference (see Figure 3.6). Where ϕ is the angle between the horizontal and the centreline of the pick point and is called the angle of attack, γ is the clearance angle which is the angle between the horizontal and the bottom of the pick, d is the cutting depth, α is half the tip angle and β is the rake angle which is defined positive when the angle leans backwards and is negative when it leans forward relative to the vertical in the cutting direction. Furthermore, compressive stresses and forces are positive, as well the tensile stresses, the tensile forces are negative.

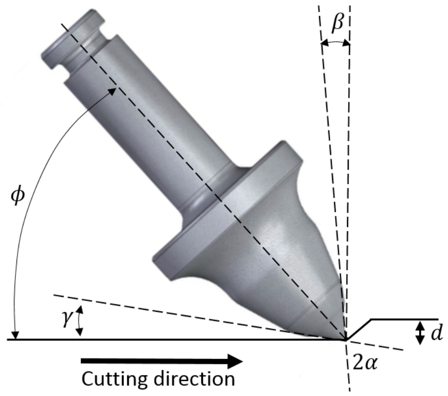

Figure 3.6: Geometry of a pick point.

Nishimatsu

The theory of Nishimatsu (1972) is based on brittle shear failure. He describes the cutting force on a chisel shaped tool similar to Merchant (1944) (1945a) (1945b) and made the following assumptions:

- The model does not incorporate a crushed zone
- Failure occurs according to a linear Mohr envelope.
- The resulting stresses acting on the failure plane A−B based on the shear angle ω in Figure 3.7 are proportional to a power n, which is the stress distribution factor. The exponent n is calculated with the following empirical relation:

$$n = 11.3 - 0.18\beta \tag{3.5}$$

Nishimatsu (1972) obtained the following equations for the peak cutting and normal forces acting on the blade:

$$PCF_{Ni} = \frac{1}{n+1}\frac{2cdw\cos(\varphi)\cos(\beta-\delta)}{1+\cos(\beta-\delta-\varphi)} \tag{3.6}$$

$$PNF_{Ni} = \frac{1}{n+1}\frac{2cdw\cos(\varphi)\sin(\beta-\delta)}{1+\cos(\beta-\delta-\varphi)} \tag{3.7}$$

Where PCF is the peak cutting force in the cutting direction, PNF is the peak normal force perpendicular to the cutting direction, w is the width of the tool, δ is the external friction angle, φ is the internal friction angle and c is the cohesive shear strength according to:

$$c = \frac{\sigma_c}{2}\frac{1-\sin(\varphi)}{\cos(\varphi)} \tag{3.8}$$

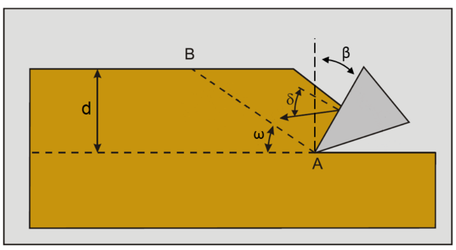

Figure 3.7: Model for shear failure by Nishimatsu (based on (Miedema, 2014)).

Evans 2D

Most of the literature on rock cutting with a theoretical approach is based on this theory of Evans (1964) and Evans and Pomeroy (1966). They forwarded a theory to calculate the cutting forces of wedge-shaped coal cutting tools that is based on brittle tensile failure. Figure 3.8 shows a schematic representation of the model, where a tensile crack occurs along the curve C-D. In the model they made the following assumptions:

- The model does not incorporate a crushed zone
- There is no friction included between the wedge and the coal
- The penetration depth is small compared to the layer thickness.

The cutting and normal forces are respectively calculated with:

$$PCF_{Evans2D} = \sigma_t dw \frac{2\sin(\alpha+\delta)}{1-\sin(\alpha+\delta)} \tag{3.9}$$

$$PNF_{Evans2D} = \sigma_t dw \frac{\cos(\alpha+\delta)}{1-\sin(\alpha+\delta)} \tag{3.10}$$

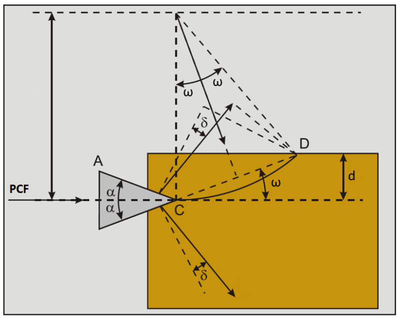

Figure 3.8: Model for tensile failure by Evans (1964) (based on Miedema (2014)).

Miedema

Hatamura and Chijiiwa (1975) identified three different failure mechanisms in the soil excavation processes: the **flow type**, the **shear type**, and the **tear type** (Figures 3.9a, 3.9b and 3.9c). Miedema (2014) derived a rock cutting model for the flow type and the tear type, which is applicable for both ductile and brittle failure of rock. Furthermore, he added two different cutting mechanisms for the excavation of rock, called the **chip type** and the **crushed type** (Figures 3.9d and 3.9e). The crushed type occurs when a thin layer of rock is scratched from the surface and is similar to the shear type. The chip type occurs when a thicker layer of rock is cut which is similar to the tear type. In deriving the rock cutting model, the following assumptions were made:

- The model does not incorporate a crushed zone
- the external friction angle δ is 2/3 of the internal friction angle φ
- The shear angle ω in the tear type is 22.5° smaller than the shear angle in the flow type.

The rock cutting model derived for the flow type is based on the the steel cutting model of Merchant (1944) and the sand cutting model of Miedema (1987). For ductile failure, the mean cutting forces are calculated with:

$$MCF_{miedema} = \frac{2cdw\cos(\varphi)\sin(\phi+\delta)}{1+\cos(\phi+\delta+\varphi)} \tag{3.11}$$

$$MNF_{miedema} = \frac{2cdw\cos(\varphi)\cos(\phi+\delta)}{1+\cos(\phi+\delta+\varphi)} \tag{3.12}$$

Where MCF is the mean cutting force in the cutting direction, MNF is the mean normal force perpendicular to the cutting direction. Miedema (2014) modified this theory for brittle failure of rock and made a distinction between brittle shear (shear type), brittle tensile (tear type) or a combination of both (chip type). The model of the flow type (Equation 3.11 and 3.12) is still applicable for calculating the forces of the shear type, however they result in the peak instead of the mean forces.

The tear type occurs if the minimum principal stress σ_{min} is smaller than the Brazilian Tensile Strength of the rock. For this case, Miedema (2014) defined a mobilized cohesive shear strength to use in Equation 3.11 and 3.12, instead of using the cohesive shear strength. The mobilized cohesive shear strength is calculated with:

$$c_m = \frac{\sigma_t}{\left(\frac{\sin(\frac{\phi+\delta-\varphi}{2})}{\cos(\frac{\phi+\delta+\varphi}{2})} - 1\right)\left(\frac{1-\sin(\varphi)}{\cos(\varphi)}\right)} \tag{3.13}$$

Furthermore, he found that the shear angle of the tear type is 22.5° smaller than the shear angle used in the shear type. Due to this change, there is a region where both shear as the tear type can occur. Here, the shear crack transfers into a tensile crack due to a decrease in stress over distance, which is called the chip type. Substituting the mobilized cohesive shear strength from Equation 3.13 into Equation 3.12 and correcting for the shear angle, the cutting and normal forces for the tear and chip type are calculated with:

$$PCF_{miedema} = \frac{2c_m dw\cos(\varphi)\sin(\phi+\delta)}{\cos(\frac{\pi}{4})+\cos(\phi+\delta+\varphi)} \tag{3.14}$$

$$PNF_{miedema} = \frac{2c_m dw\cos(\varphi)\cos(\phi+\delta)}{\cos(\frac{\pi}{4})+\cos(\phi+\delta+\varphi)} \tag{3.15}$$

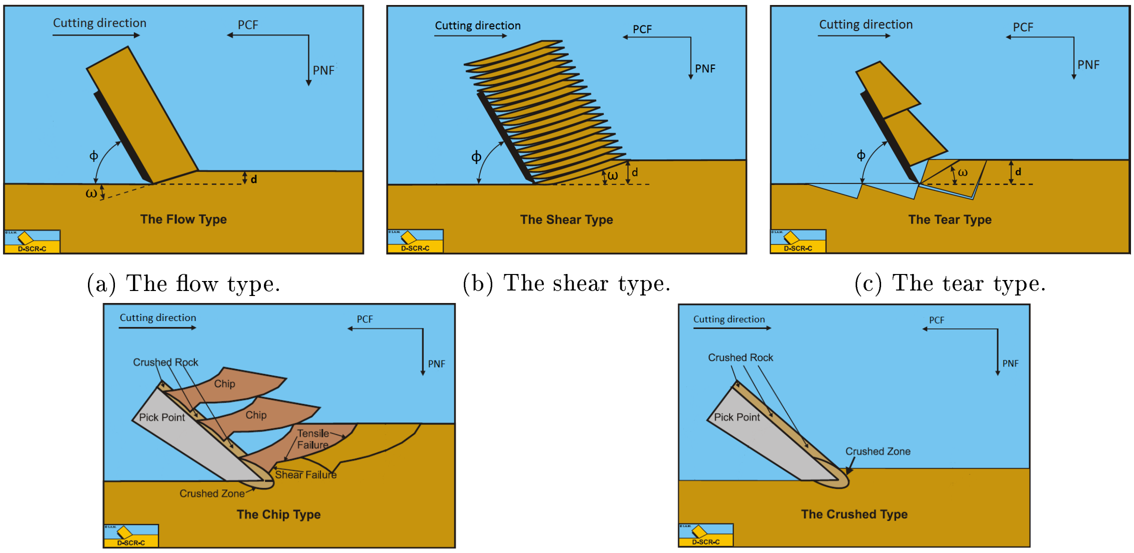

(a) The flow type. (b) The shear type. (c) The tear type.

(d) The chip type. (e) The crushed type.

Figure 3.9: Different types of cutting mechanism (based on Miedema (2014)).

Evans 3D

The models Evans and Pomeroy (1966), Nishimatsu (1972) and Miedema (2014) describe are all two dimensional and applicable for wedge-shaped tools. However, during rock excavation, often pick points are used which behaviour is essentially three-dimensional. (Evans, 1984) incorporated this three-dimensional physical behaviour. and made some simplification by making the following assumptions:

- The conical pick penetrates parallel to the surface
- The pick is subjected to internal pressure (Figure 3.10).
- Tensile cracks occur when the stress equals the tensile stress of the rock.

To calculate the peak cutting force (PCF), Evans (1984) derived the following equation:

$$PCF_{Evans3D} = \frac{16\pi\sigma_t^2 d^2}{\cos(\alpha)^2 \sigma_c} \tag{3.16}$$

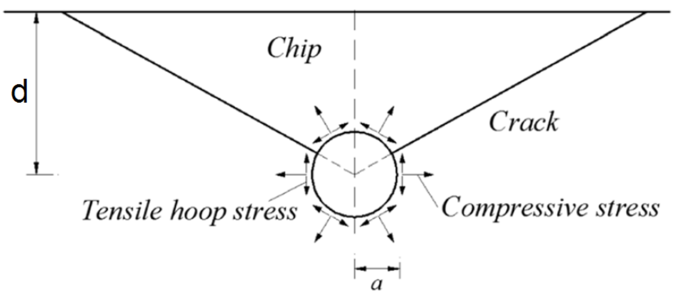

Figure 3.10: Hole under internal pressure (Evans, 1984).

Goktan

Goktan (1997) modified the model of Evans (1984), because it has some deficiencies:

- The cutting force does not reduce to zero when $\alpha = 0$ although it should.
- The cutting force is inversely proportional to the compressive strength of the rock, which is not the case in practice.

the modified formula of Evans (1984) by Goktan (1997) is given by:

$$PCF_{Goktan} = \frac{4\pi\sigma_t d^2 \sin^2(\alpha + \delta)}{\cos(\alpha + \delta)} \tag{3.17}$$

Where δ is the friction angle between the pick and rock, which he assumed as 8.5°.

The modification is still based on a circular hole bored parallel to the surface (Figure 3.10), but in reality the cutting mechanism of rock breaking is under an asymmetrical attack (Figure 3.6). Goktan et al. (2005) included the parameter rake angle β and modified it towards a semi-empirical formula where the tip angle α is assumed to be 90°. A close fit to full-scale linear rock cutting experiments was obtained by:

$$PCF_{Goktan2005} = \frac{12\pi\sigma_t d^2 \sin^2[\frac{1}{2}(90 - \beta) + \delta]}{\cos[\frac{1}{2}(90 - \beta) + \delta]} \tag{3.18}$$

Li

Li et al. (2018) proposed a model based on the energy and stress criteria of Griffith's fracture mechanics theory (Griffith and Eng, 1921) for calculating the forces on a pick point.

This approach differs from the previous models which are all based on calculating the force during the crack formation. They stated that it is more likely that the peak cutting force occurs in the initiation phase of the rock cutting process with the formation of a crushed zone. The importance of this zone in the rock cutting process has been confirmed by Mishnaevsky (1995), who expects that up to 90% of the energy is spent in rock crushing near the tip. To determine the peak cutting force, Li et al. (2018) made the following assumptions in his model:

- The stress increases linearly with the cutting depth across the conical surface
- The direction of the stress is perpendicular to the conical surface.
- The elliptical profile at section A−A is simplified to a circle as shown in figure 3.11b

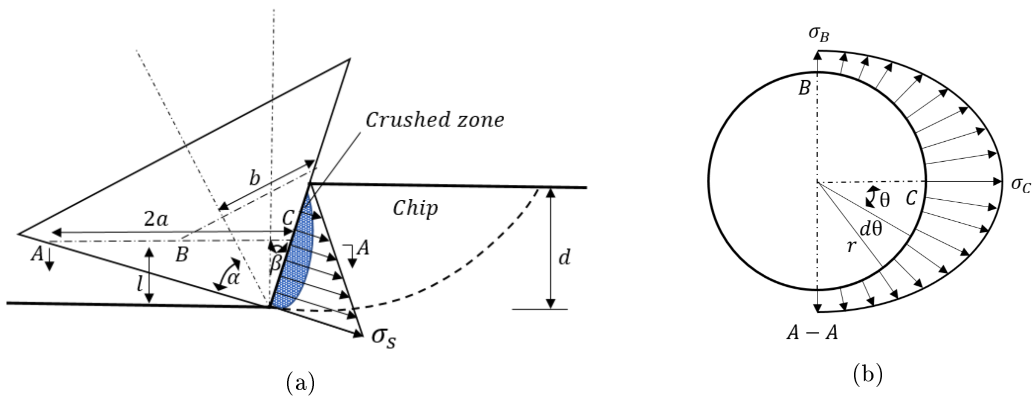

Figure 3.11: The schematic of stress distribution on the conical pick based on Li et al. (2018).

For calculating the peak cutting force, the stress is integrated along the surface of the pick point with:

$$\begin{aligned} PCF_{Li} &= \int_0^d \int_{-\pi/2}^{\pi/2} \left[\frac{2}{\pi}\left(\frac{\sin(\alpha)}{\cos(\beta)} - 1\right)\theta + 1\right] \frac{(d-l)K_{Ic}}{d\sqrt{\pi\delta_{li}}} \cos(\theta)\lambda l d\theta dl \\ &= \frac{\lambda_{li} K_{Ic} d^2}{3\sqrt{\pi\delta_{li}}} \end{aligned} \tag{3.19}$$

Where l is the distance between the horizontal profile and the pick tip, θ is the angle between a point on the circle and the cutting direction as shown in Figure(3.11b) and δ_{li} is the crack length. The full derivation according to Li et al. (2018) can be found in Appendix A.

Li et al. (2018) noted that the stress on the pick is negatively correlated with the size of the crack δ_{li}. They assumed that the stress acting on the pick is largest at the crack initiation and decreases as the crack propagates. They concluded that the peak cutting force occurs at the crack initiation and decreases as the crack propagates until the chip is separated from the rock.

K_{Ic} is the fracture toughness of the rock, which can be determined by the empirical relation obtained by Kahraman and Altindag (2004):

$$K_{Ic} = 0.11(\frac{\sigma_c \sigma_t}{2})^{0.43} \tag{3.20}$$

λ_{li} is a constant that depends on the tip angle α and rake angle β of the pick point and is calculated with:

$$\lambda_{li} = \frac{\tan(2\alpha - \beta) + \tan(\beta)}{4} + \frac{1}{2}\tan(\alpha)\left[\frac{\tan(2\alpha - \beta) - 2\tan(\alpha - \beta) - \tan(\beta)}{2}\sin(\alpha - \beta) + \frac{1}{\cos(\alpha - \beta)}\right] \tag{3.21}$$

For calculating the crack length, the energy criterion of Griffith's fracture theory is used. It determines the amount of energy needed for creating a crack of a certain length. The work done by the pick or elastic energy stored in the rock should be greater or equal to the energy needed for the crack:

$$U_0 \geq G_S \tag{3.22}$$

Where U_0 is the work done by the pick point and G_s is the energy needed for generating the new surface during crack propagation according to Griffith and Eng (1921). Applying the Griffith's energy criterion for crack growth, the surface energy for generating a crack of length δli is calculated with:

$$G_S = \pi\delta_{li}^2\gamma_{li} = \frac{\pi\delta_{li}^2 K_{Ic}^2}{2E} \tag{3.23}$$

Where G_S is the energy needed in [J]. The work done by the pick is stored in the rock as elastic energy until the crack is initiated according to the linear elastic fracture mechanics Griffith and Eng (1921). The work done by the pick is:

$$\begin{aligned} U_0 &= \int \Delta U dA = \int_0^d \int_{-\pi/2}^{\pi/2} \frac{\sigma^2}{2E} r d\theta \frac{dl}{\cos(\beta)} \\ &= \frac{\lambda_{li} K_{Ic}^2 d^2}{24E\delta_{li}\cos(\beta)}\left[\frac{1}{3}\left(\frac{\sin(\alpha)}{\cos(\beta)} - 1\right)^2 + 1\right] \end{aligned} \tag{3.24}$$

Where U_0 is the amount of work in [J/m]. Noted is that the Equation 3.22 is dimensionally incorrect, as the left part of the equation is the amount of energy needed for generating a crack of length δ_{li} in [J] and the right part of the equation is the amount of work needed to initiate the crack in [J/m]. Not all the steps within the derivation of Li et al. (2018) were given, which makes it uncertain to determine if there is made an assumption to fit the theoretical model, resulting in a semi-empirical equation.It is assumed that the difference in dimension can be regarded due to the fact that Griffith's energy criterion is mainly based on a 2D problem. However, the derivation of Li et al. (2018) is applied on a 3D problem, which gives the possibility to believe that the theoretical derivation of Li et al. (2018) assumes that the 2D model is valid for the 3D problem which can explain the difference in the dimension [m]. According to Li et al. (2018), combining Equations 3.22, 3.23 and 3.24, the size of the crack, , when it is initiated becomes:

$$\delta_{li} = \sqrt[3]{\frac{\lambda_{li} d^2}{12\pi\cos(\beta)}\left[\frac{1}{3}\left(\frac{\sin(\alpha)}{\cos(\beta)} - 1\right)^2 + 1\right]} \tag{3.25}$$

Where δ_{li} is the crack length given in [m].
The peak cutting force is calculated by combining Equation 3.19 with 3.25:

$$PCF_{Li} = \frac{\lambda_{li}^{\frac{5}{6}} K_{Ic} d^{\frac{5}{3}}}{3\sqrt[6]{\frac{\pi^2}{12\cos(\beta)}\left[\frac{1}{3}\left(\frac{\sin(\alpha)}{\cos(\beta)} - 1\right)^2 + 1\right]}} \tag{3.26}$$

In order to make the equation dimensionally correct, a correction factor X with a value of 1 and a dimension [m] is added to the formula which results in the following equation:

$$PCF_{Li} = \frac{\lambda_{li}^{\frac{5}{6}} K_{Ic} d^{\frac{5}{3}}}{3\sqrt[6]{\frac{X\pi^2}{12\cos(\beta)}\left[\frac{1}{3}\left(\frac{\sin(\alpha)}{\cos(\beta)} - 1\right)^2 + 1\right]}} \tag{3.27}$$

3.2.3 Empirical relations rock cutting

Empirical relations between the cutting force and rock type are obtained by doing linear rock cutting experiments. Doing such type of experiments is time costly, expensive and there are only a few laboratories in the world that can succeed them, which leads to a lot of confidential data. One of the few public experimental datasets is described by Copur et al. (2003) and is given in Appendix B.

Bilgin

Bilgin et al. (2006) describe the full scale linear rock cutting experiment from Copur et al. (2003). The set-up of the experiment is shown in Figure B.1. Bilgin et al. (2006) carried out a statistical analysis based on 22 measurements to obtain a relation between the cutting forces and the rock properties. The best correlations are obtained with the UCS value of rock, suggesting that this is the most important property affecting the performance of conical picks. Empirical relations obtained for calculating the mean forces in [kgf] based on the UCS value in [MPa] are:

$$MCF_{Bilgin} = (0.826\sigma_c + 58.53)d\cdot \tag{3.28}$$

$$MNF_{Bilgin} = 1.217\sigma_c^{1.014}d\cdot \tag{3.29}$$

Bilgin et al. (2006) found a factor of 2.69 $\pm$ 0.32 between the peak and the mean forces for unrelieved cutting, which results in the following formulas for the peak cutting forces:

$$PCF_{Bilgin} = (2.222\sigma_c + 21.76)d \tag{3.30}$$

$$PNF_{Bilgin} = 3.274\sigma_c^{1.014}d \tag{3.31}$$

In both equations, the force increases linearly with the cutting depth, while according to brittle rock failure in Figure 3.5, a non-linear relationship is observed, were the forces tend to become constant with increasing depth. Furthermore, the equations are valid for a cutter with an tip angle of 80° and the dimensions of the equations are not correct, which makes it unreliable to extrapolate the equations for input variables which are not used during the experiment.

The empirical relations are only valid for estimating cutting forces on a pick point for a single cut (unrelieved). However, during drilling, pick points are placed in an array where there is interaction between the groves, resulting in a relieved cutting condition. The tool forces in relieved cutting are lower than those in unrelieved cutting. Bilgin et al. (2006) describe also relieved cutting experiments. They stated that the cutting forces in relieved mode are not possible to estimate theoretically. Empirical relations obtained for calculating the mean forces in [kgf] based on the UCS value in [MPa] were found:

$$MCF_{Bilgin_{rel}} = 2.347\sigma_c^{0.785}d \tag{3.32}$$

$$MNF_{Bilgin_{rel}} = 0.752\sigma_c^{1.051}d \tag{3.33}$$

A factor of 3.07 $\pm$ 0.55 between the peak and the mean forces for relieved cutting, which results in the following formulas for the peak cutting forces:

$$PCF_{Bilgin_{rel}} = 7.205\sigma_c^{0.785}d \tag{3.34}$$

$$PNF_{Bilgin_{rel}} = 2.309\sigma_c^{1.051}d \tag{3.35}$$

3.2.4 Validation rock cutting models

To validate the linear rock cutting models, the models are compared with experimental data of Copur et al. (2003). During the tests the mean and peak forces in the cutting and normal direction perpendicular to the cutting direction were measured. In Appendix B, the unrelieved peak cutting forces from the experiments are compared with the peak cutting forces obtained with the models and summarized in table 3.2. The first column shows the type of model. To compare the theoretical models quantitatively, the mean relative deviation is calculated in the second column with:

$$\epsilon = \frac{100}{N} \sum_{i=1}^{N} \frac{|PCF_{theory} - PCF_{experiment}|}{PCF_{experiment}} \tag{3.36}$$

Where PCF_{theory} is the theoretical calculated value for the peak cutting force, $PCF_{experiment}$ is the peak cutting force value obtained by experiments and N is the number of samples tested.

The deviation in percentage from the mean is given in the third column shows if the model over or underestimate the experiments with:

$$\epsilon_a = \frac{100}{N} \sum_{i=1}^{N} \frac{PCF_{theory} - PCF_{experiment}}{PCF_{experiment}} \tag{3.37}$$

All models underestimate the experiments. For the first five models, the deviation equals the mean relative deviation, because all the theoretical values are below the experimental values. Furthermore, a statistical analysis is done by calculating the correlation coefficient between the experiment and the model, which is used to measure the strength of a linear association between two variables, where a coefficient of 1 means a perfect positive correlation. The coefficient in the fourth column can be determined with:

$$r_c = \frac{n(\Sigma PCF_{theory} PCF_{experiment}) - (\Sigma PCF_{theory})(\Sigma PCF_{experiment})}{\sqrt{[n\Sigma PCF_{theory}^2 - (\Sigma PCF_{theory})^2][n\Sigma PCF_{experiment}^2 - (\Sigma PCF_{experiment})^2]}} \tag{3.38}$$

Where r_c is the correlation coefficient.

From Table 3.2 is concluded that the theory of Li et al. (2018) gives the best results compared with the other theoretical models. The mean relative deviation is around 26% and the average is approximately 22% below the experimental values and the correlation coefficient is the closest to 1. The empirical relation of Bilgin et al. (2013) calculates the experiments based on the average and mean relative deviation better than the theoretical model of Li et al. (2018), but is questionable when the variables of the experiment changes.

Table 3.2: Summary of the linear rock models compared with peak cutting force values from the experiments of Copur et al. (2003).

Theory	**Mean relative deviation** [%]	**Average** [%]	**Correlation coefficient** [-]
Nishimatsu (1972)	98	-98	0.89
Evans and Pomeroy (1966)	92	-92	0.89
Miedema (2014)	93	-93	0.89
Evans (1984)	87	-87	0.70
Goktan (1997)	83	-83	0.89
Goktan et al. (2005)	34	-29	0.89
Li et al. (2018)	26	-22	0.91
Bilgin et al. (2006)	25	-12	0.89

So far, the models are compared with the peak cutting force of the experiment. However, during the rock cutting process, the mean cutting force determines the amount of torque needed to rotate the drill.

A close fit with the mean cutting forces of the experiments of Copur et al. (2003) is found by dividing the peak cutting force of Li et al. (2018) by 2.25 (Appendix B). A summary of the results is given in Table 3.3.

Table 3.3: Summary of the linear rock models compared with mean cutting force values from the experiments of Copur et al. (2003).

Theory	**Mean relative deviation**	**Average**	**Correlation coefficient**
	[%]	[%]	[-]
Li et al. (2018)	27	-0.2	0.91
Bilgin et al. (2006)	26	-8	0.88

3.2.5 Conclusion linear rock cutting theory

Due to the complex mechanism of the rock cutting process it is not possible to match all the experimental results and it is still a challenge to build more reliable models. Many parameters can have a significant influence on the forces that occur during the rock cutting process and the rock cutting process is still not fully understood.

The influence of the cutting depth on the cutting force differs per model. Li et al. (2018) derived that the cutting force increases by $d^{5/3}$, while others found a relation with d^2. According to Bilgin et al. (2006) the relation is linear. Looking at Figure 3.5, a non-linear relationship is observed, were the cutting forces in brittle rock tend to become constant with increasing depth. This phenomena makes the applicable of the cutting models questionable at large cutting depths.

More reliable results may be obtained by including more variables in the equations which are related to the rock cutting process. Even when this increases the accuracy of the model, it also increases the complexity of the model. Often, only a limited amount of data available before cutting rock. Therefore, the use of a model requires a minimum amount of input that can predict the outcome reasonably well. For estimating the mean cutting force theoretically, the model of Li et al. (2018) gives the best agreement with the experimental values with a mean relative deviation of 27%. However, this model may not be valid for ductile failure of rock and does not incorporate an effect for relieved cutting. A summary of the described linear cutting models is given Table 3.4 according to model, cutting type and input parameters.

Table 3.4: Summary of the linear cutting models.

Theory	**Model**	**Failure mechanism**	**Input**
Nishimatsu (1972)	Semi-empirical 2D	Brittle shear	$n, c, d, w, \varphi, \beta, \delta,$
Evans and Pomeroy (1966)	Theoretical 2D	Brittle tensile	$\sigma_t, d, w, \alpha, \delta$
Miedema (2014)	Theoretical 2D	Ductile, brittle tensile, brittle shear	$c, d, w, \varphi, \phi, \delta, \sigma_t$
Evans (1984)	Theoretical 3D	Brittle tensile	$\sigma_t, d, \alpha, \sigma_c$
Goktan (1997)	Theoretical 3D	Brittle tensile	$\sigma_t, d, \alpha, \delta$
Goktan et al. (2005)	Semi-empirical 3D	Brittle tensile	$\sigma_t, d, \beta, \delta$
Li et al. (2018)	Semi-empirical 3D	Brittle tensile	$d, \beta, \alpha, \sigma_c, \sigma_t$
Bilgin et al. (2006)	Empirical 3D	-	σ_c, d

3.3 Rock indentation theory

Rock excavation by indenters differs from excavating rock with cutting tools. Instead of making a horizontal cutting action, they roll over the surface and indent the rock vertically. Normally roller bits are used for the indentation of rock as described in paragraph 2.3.2. The next sections describe the physical phenomena, the existing (semi-)theoretical and empirical rock indentation models for a single indenter and the existing models used for the calculation of the forces on a roller bit.

3.3.1 Physical phenomena rock indentation theory

During the indentation of the rock, the failure modes can be either ductile or brittle, which can be determined with the ductility number as defined in Equation 3.1. Indenting ductile rock gives a smooth function of the force over penetration depth. The expected force over penetration depth depends only on the indenters geometry when the rock does not increase or decrease in strength during the indentation. Figure 3.12 shows the penetration curves for the following indenters:

A Flat-face indenter.

B Two dimensional wedge.

C Cone or pyramid.

D Cylindrical bearing.

E Spherical indenter.

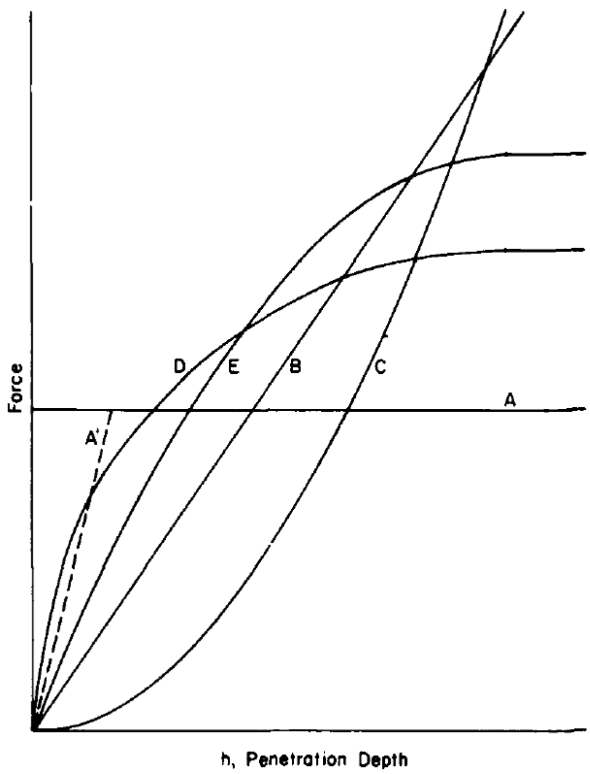

Figure 3.12: Expected force penetration graphs for indenting ductile material (Mellor, 1980).

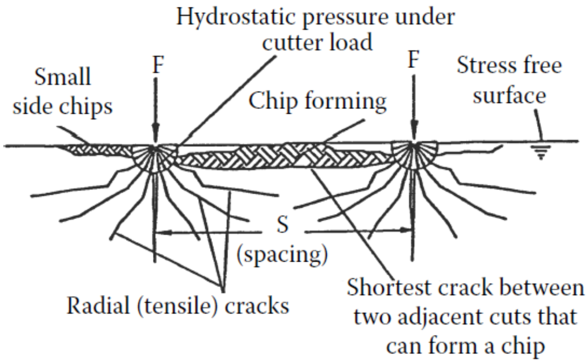

Figure 3.13: Chip forming process indentation tools(Bilgin et al., 2013).

Roller bits are not favourable for the excavation of ductile rock, because the removed area by the indenter is only slightly larger than the penetrated volume of the indenter. In brittle rock, the removed area is larger due to the formation of rock chips. As the force increases and the indenter penetrates, cracks start to form which leads to the break out of rock chips (Figure 3.13). During the break out, a decrease in force is observed as is shown in Figure 3.14. Often a line is drawn through the peaks of every chipping stage, which is taken equivalent to the continuous penetration curve that would be obtained during indenting of a ductile material. Linear force penetration envelopes have been accepted as good approximations for a number of materials subjected to both ductile and brittle penetration by wedges and spheres. The slope of this envelope is often called the penetration index. This value can be used directly in the formulas for predicting drilling rate. According to Bilgin et al. (2013), the penetration indices for a single indenter, having a tip radius of 3 mm, in different UCS ranges are given in Table 3.5.

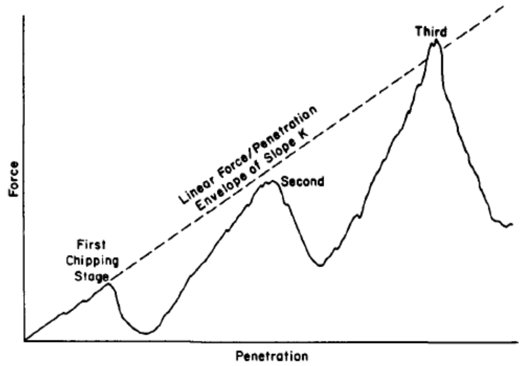

Figure 3.14: Typical force penetration graph for indenting brittle material (Mellor, 1980).

Table 3.5: Penetration index values for different types of rock (Bilgin et al., 2013).

Unconfined Compressive Strength $[MPa]$	**Penetration Index grain size <3 mm** $[kN/mm]$	**Penetration Index grain size >3 mm** $[kN/mm]$
30-80	15-20	15-20
80-150	20-30	20-25
150-250	30-40	25-35

3.3.2 Theoretical and semi-empirical rock indentation models

This section describes the theoretical based models of Evans and Pomeroy (1966), Paul and Sikarskie (1965) Miller and Sikarskie (1968) and Roxborough and Phillips (1975) to determine the relation between the force and penetration depth into brittle rock for a various number of indenters.

Paul & Sikarskie

Paul and Sikarskie (1965) studied the theory of the penetration a two dimensional wedge into brittle rock based on the Mohr Coulomb failure criteria:

$$\tau = c + \sigma_n \tan(\varphi) \tag{3.39}$$

Where τ is the shear strength, σ_n is the normal stress, c is the cohesion and φ the internal friction coefficient.
They assumed:

- Chips form repeatedly along a failure surface with a constant break-out angle (Figure 3.15) defined by:
$$\psi = \frac{1}{2}\left[\left(\frac{\pi}{2}\right) - \left(\frac{\alpha + \varphi}{2}\right)\right] \tag{3.40}$$
- The force penetration curve during the formation of the chip is linear.
- There is no friction between the wedge and material.

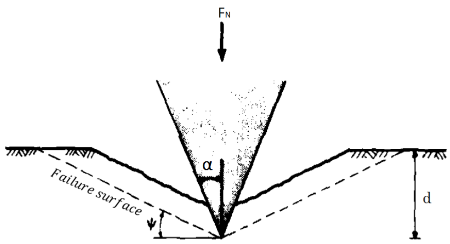

Figure 3.15: Break out wedge according to Paul and Sikarskie (1965).

Taking a linear envelope for force-penetration relation resulted in the following formula:

$$F_N = \frac{2d \tan(\alpha)\cos(\alpha)(1 - \sin(\varphi))}{1 - \sin(\alpha + \varphi)}\sigma_c = 2d\tan(\alpha)B_1\sigma_c \tag{3.41}$$

A limitation of the formula is that the penetration force F_N becomes infinitely large when $\alpha + \varphi = \frac{\pi}{2}$. Paul and Sikarskie (1965) stated that this limit is a boundary between two failure modes. When $\alpha + \phi < \frac{\pi}{2}$, the rock fails by crushing and chipping and when the summation of the angles $> \frac{\pi}{2}$, the rock fails only by crushing. For simplicity, Equation 3.41 can be rewritten in the bearing surface of the indenter multiplied the UCS value σ_c times a term B_1.

Evans

Evans and Pomeroy (1966) summarized the research done towards the penetration of wedges into coal. They assumed:

- The force is proportional to the surface bearing area of the wedge:
$$A_{tooth} = 2dw\tan(\alpha) \tag{3.42}$$

- The critical normal stress σ_n equals the unconfined compressive strength σ_c of coal.

Which leads to the following equation to calculate the penetration force:

$$F_N = 2dw\tan(\alpha)(1+\mu(\alpha))\sigma_c = A_{tooth}B_2\sigma_c \tag{3.43}$$

Where μ is the friction coefficient between steel and coal, which is approximately 0.5, but depends on the half tip angle α. The formula of Evans and Pomeroy (1966) rewritten in the bearing surface of the indenter multiplied the UCS value σ_c times a term B_2, which is can have values between 1 and 3.

Miller & Sikarskie

Miller and Sikarskie (1968) extended the model of Paul and Sikarskie (1965) for three dimensional indenters such as cones and pyramids. For a cone (Figure 3.16), the equation becomes:

$$F_N = \frac{A_{cone}\sin(\alpha)\cos(\varphi)c}{\cos(\psi+\alpha+\varphi)} \tag{3.44}$$

Where A_{cone} is the indented area of of the cone which can be calculated with:

$$A_{cone} = \pi d^2 \frac{\cos(\psi)}{\sin(\psi)^2} \tag{3.45}$$

The formula can be written in the bearing surface of the indenter multiplied by a term $B3$ and the UCS value σ_c. B_3 depends on the half tip angle α, internal friction angle of φ and the break out angle ψ:

$$F_N = \pi d^2 \tan(\alpha)^2 \frac{\cos(\psi)\cos(\alpha)^2(1-\sin(\varphi))}{2\sin(\alpha)\sin(\psi)^2\cos(\psi+\alpha+\varphi)}\sigma_c = A_{cone}B_3\sigma_c \tag{3.46}$$

Miller and Sikarskie (1968) used a different formula for calculating the break out angle ψ than Paul and Sikarskie (1965), given in Equation 3.40, which they only showed graphically in Figure 3.17.

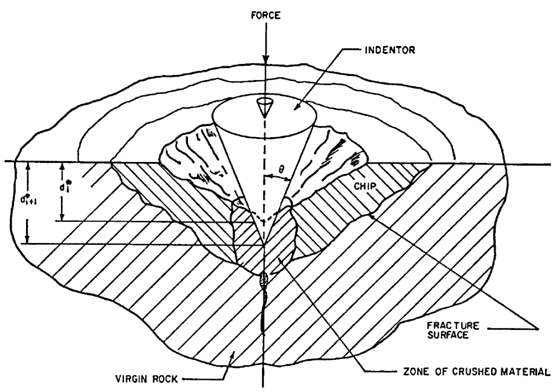

Figure 3.16: Indentation of rock by a three dimensional indenter (Miller and Sikarskie, 1968).

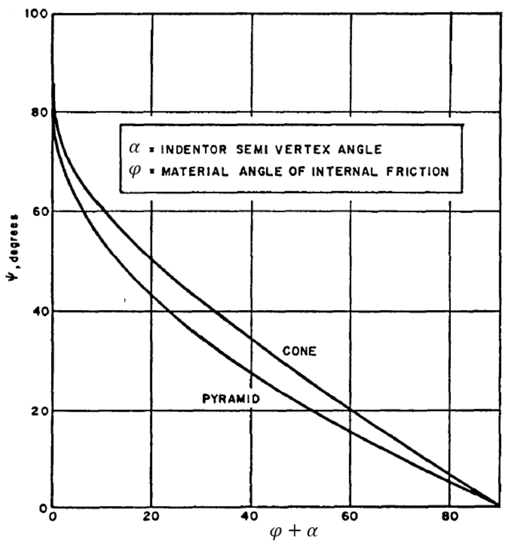

Figure 3.17: Break out angle according to Miller and Sikarskie (1968).

Roxborough and Phillips

Roxborough and Phillips (1975) used a simple mathematical model to calculate the normal, rolling and side forces on a single V-shaped cutter disc. They assumed that the mean thrust force equals the UCS multiplied with the projected area of the bearing surface:

$$F_N = \sigma_c A_{disc} \tag{3.47}$$

The projected area of the bearing surface can be approximated with:

$$A_{disc} = lw \tag{3.48}$$

Where l is the chord length of the disc and w the width of the disc at the indentation depth. The chord length can be calculated easily by using the ABC formula:

$$l = 2\sqrt{2rd - d^2} \tag{3.49}$$

Where r is the radius of the disc. The width of the disc depends on the the V-shape angle and is calculated with:

$$w = 2d\tan(\alpha) \tag{3.50}$$

With the chord length and the width known, the bearing surface A becomes:

$$A_{disc} = 4d\tan(\alpha)\sqrt{2rd - d^2} \tag{3.51}$$

Inserting equation 3.51 into equation 3.47 the penetration force becomes:

$$F_N = 4\sigma_c \tan(\alpha) d\sqrt{2rd - d^2} = F_N = A_{disc} B_4 \sigma_c \tag{3.52}$$

During drilling, the disc rolls over the surface instead of being pushed into vertically. Roxborough and Phillips (1975) made the assumption that the calculated value for the thrust force is still valid for the rolling disc (Figure 3.18). Experiments showed that the peak values of the rolling conditions are substantially the same as force obtained in the static conditions (Figure 3.19).

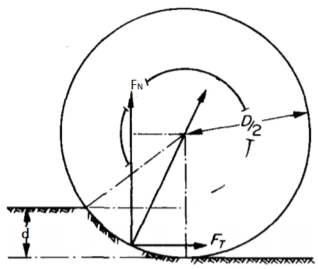

Figure 3.18: Rolling disc by Roxborough and Phillips (1975).

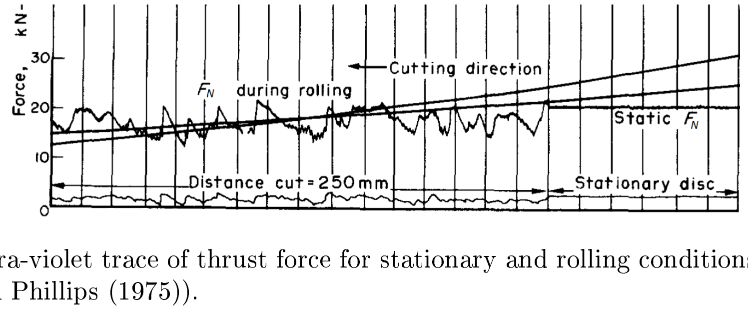

Figure 3.19: Ultra-violet trace of thrust force for stationary and rolling conditions (modified from Roxborough and Phillips (1975)).

3.3.3 Empirical rock indentation models

Wijk

A test that is often linked to the prediction of drilling rates with indenters is called the Stamp test, described by Wijk (1989). During the test, a rigid circular indenter of radius b is pressed into a flat rock surface as shown in Figure 3.20. First the indenter penetrates the rock elastically, but at a certain load a crushed zone appears under the indenter which leads to the formation of tensile cracks. Further penetration lets the cracks propagate to the surface which leads to the break out of chips. During this process, a peak force F_N is required for the crack initiation. Together with the geometry of the indenter the stamp strength is defined as:

$$\sigma_{st} = \frac{F_N}{\pi b^2} \tag{3.53}$$

Where b is the radius of the indenter and F_N is the peak force required for the crack initiation. The stamp strength is found to be much higher than the unconfined compressive strength, because in the stamp test the rock sample is virtually in semi-infinite state compared with an UCS test where the rock sample is a cylinder. According to Wijk (1992) and other researchers there is a ratio between the stamp strength and the unconfined compressive strength which can vary between:

$$3 \geq \frac{\sigma_{st}}{\sigma_c} \leq 10 \tag{3.54}$$

They observed by experiments that the stamp strength ratio $\frac{\sigma_{st}}{\sigma_c}$ normally decreases with an increasing contact area of the indenter.

Furthermore, Wijk studied the theory of drilling with roller bits (Wijk, 1992). He stated that a large diameter drill head equipped with rollers may be seen as one gigantic roller bit. Here, the peak indentation forces occur at a different time interval, which leads to the mean penetration forces for determining the amount of thrust. The total contact area with the rock is much larger than the grain size of the rock and homogeneous behaviour of the rock is expected. Wijk (1992) assumed that this phenomena results in a decrease in ratio between the stamp strength and unconfined compressive strength to approximate 3. The assumption matches reasonably well with the tunnel boring experiments of Wagner and Schümann (1971). Where a value of approximately 3 was found for a large number of discs penetrating simultaneously into the rock. The formula for calculating the penetration force roller bits on a large diameter drill becomes:

$$F_N = 3\sigma_c A_{indent} \tag{3.55}$$

Where A_{indent} is the indented area of the roller bits.

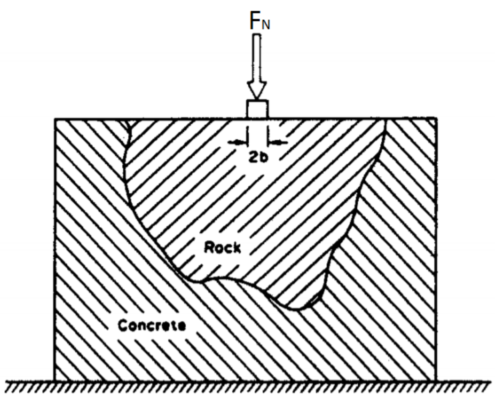

Figure 3.20: Stamp test according to (Wijk, 1989).

Warren

Warren et al. (1984) made a torque relationship based for calculating the tangential force on a roller bit. They stated that the torque is largely depending on the applied thrust on each bit and the depth of indentation. They assumed that a roller bit which consists of multiple teeth can be simplified to a disc where the tangential force is obtained by:

$$F_T = F_N \frac{\sqrt{2dr - d^2}}{r - d} \tag{3.56}$$

Where F_T is the tangential force on the roller bit, F_N is the normal force on the bit, d is the depth of the tooth and r is the radius of the bit as shown in Figure 3.21.

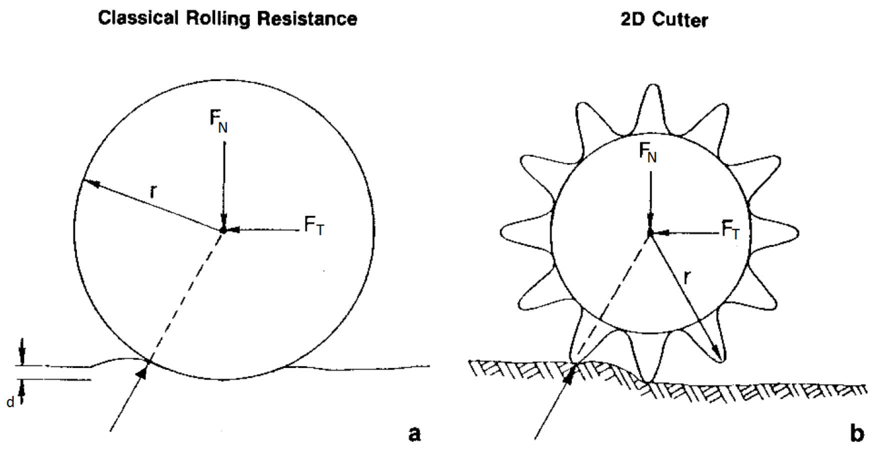

Figure 3.21: Simplification for calculating the Rolling Force by Warren et al. (1984).

Home

Home et al. (1978) made an estimation for the tangential force on a roller bit that consist of buttons. Button bits contain often more than 100 button inserts, which makes the assumption of Warren et al. (1984), to simulate the bit as a disc, questionable. Home et al. (1978) stated that the rolling force equals the penetration force times a friction constant:

$$F_T = f F_N \tag{3.57}$$

Where f is the friction constant which is approximated from experiments as 0.08 for roller bits with buttons inserted.

3.3.4 Validation rock indentation models

All the models described here, can be expressed in a way that the peak penetration force is proportional to the projected area of the bearing surface multiplied by the critical normal stress σ_n of the material. The critical normal stress equals the UCS value of the rock multiplied by a dimensionless parameter B. In Table 3.6, the value of B is given for the theoretical models, assuming a tip angle of 30° and an internal friction coefficient of 30°.

The values of B for a single indenter are in the range of $1 - 10$, except from the value obtained by Miller and Sikarskie (1968). A reason for this high value it can be found in the assumption that the stress exceeds the Mohr-Coulomb failure criterion along the whole fracture surface, but in reality, it is more likely that the stress exceeds the failure criterion at the boundary of the crushed zone that occurs underneath the indenter. From this boundary, cracks are initiated and grow in size till a chip is formed.

So far, only one indenter is taken into account for calculating the penetration force but during drilling, multiple bits on a roller bit penetrate the rock at the same time. This causes interaction between the bits and makes the application of the indentation theory for single indenter questionable. Due to the formations of cracks between the bits, rock chips are generated which cause a reduction in force. Furthermore, the mean indentation force is needed which reduces the total amount of thrust even further. On the other hand, rock chips are not directly removed underneath the cutter head, which causes regrinding of the chips into smaller particle and increases the force. Not much validation data is found that describes the behaviour of a full roller bit into rock, besides from the observations of Wijk (1989) and Wagner and Schümann (1971). Who stated that the value of B for large diameter drills tends to a value of 3.

Table 3.6: B value for calculating the peak indentation force on a single indenter according to different indentation theories.

Theory	**Model**	**Type**	**B**
Paul and Sikarskie (1965)	Theoretical	Two dimensional wedge	3
Evans and Pomeroy (1966)	Theoretical	Three dimensional wedge	$1-3$
Miller and Sikarskie (1968)	Theoretical	Three dimensional cone	17
Roxborough and Phillips (1975)	Theoretical	V-shaped rolling disc disc	2
Wijk (1991)	Empirical	Penetration test	$3-10$

3.3.5 Conclusion rock indentation theory

Many researchers tried to get a theoretical model for calculating the forces on indentation tools based on several rock parameters. The models described here can be expressed in a way that penetration force is proportional to the projected area of the bearing surface times a dimensionless constant multiplied by the UCS value. According to Wijk (1991), the value can be taken as 3 for the application in large diameter drills.

For calculating the rolling forces on the bits Warren et al. (1984) derived a model which is applicable for toothed roller bits and v-shaped disc. For calculating the rolling force on a button cutter, the empirical relation of Home et al. (1978) can be used.

Finally Table 3.7 gives a summary of the described indentation models is this section.

Table 3.7: Summary of the described indentation theories.

Theory	**Model**	**Type**	**Input**
Paul and Sikarskie (1965)	Theoretical	Two dimensional wedge	$d, \alpha, \varphi, \sigma_c$
Evans and Pomeroy (1966)	Theoretical	Three dimensional wedge	$d, w, \mu, \alpha, \sigma_c$
Miller and Sikarskie (1968)	Theoretical	Three dimensional indenters	$d, \alpha, \varphi, \psi, \sigma_c$
Roxborough and Phillips (1975)	Theoretical	V-shaped disc	d, α, r, σ_c
Wijk (1989)	Empirical	Penetration test	$b, \sigma_c,$
Warren et al. (1984)	Theoretical	Tooth cutter, disc test	d, F_N, r, σ_c
Home et al. (1978)	Empirical	Button cutter	F_N, f

4 | Drilling model

In this chapter, the model approach is presented. First an overview of the model is shown. Secondly, the excavation model is described to determine excavation limit. Finally, the transport model is presented for an airlift system that is able to calculate the transportation limit.

4.1 Model approach

In order to predict the drilling rate, a model has been developed as shown in Figure 4.1. The model calculates the rate of penetration that can be limited by either the rock excavation or transportation process. Both processes are individually modelled in a excavation model and a transport model. The model with the lowest rate of penetration defines the drilling rate. The input parameters for both models are divided into: rock characteristics, drill head characteristics and operational parameters.

The excavation model calculates the rock excavation limit, where model makes a distinction between cutting tools (pick points) and indentation tools. The calculation procedure for determining the rate of penetration is divided into steps which are regardless of the excavation mechanisms (section 4.2). Each step follows his own calculation procedure which depends on the type of mechanism. In section 4.2.1 and 4.2.3, the procedures for pick points and toothed cutters are presented. The calculation procedure for button cutters and v-shaped disc cutters is similar to the procedure for toothed cutters and therefore only the modifications are presented in section 4.2.4.

The transport model calculates the maximum number of cuttings that are able to transported with an airlift system. The model uses an airlift model that solves the momentum balance over the vertical and uses the cutting sizes obtained from the excavation model.

Both models have to be checked to see which model limits the drilling rate.

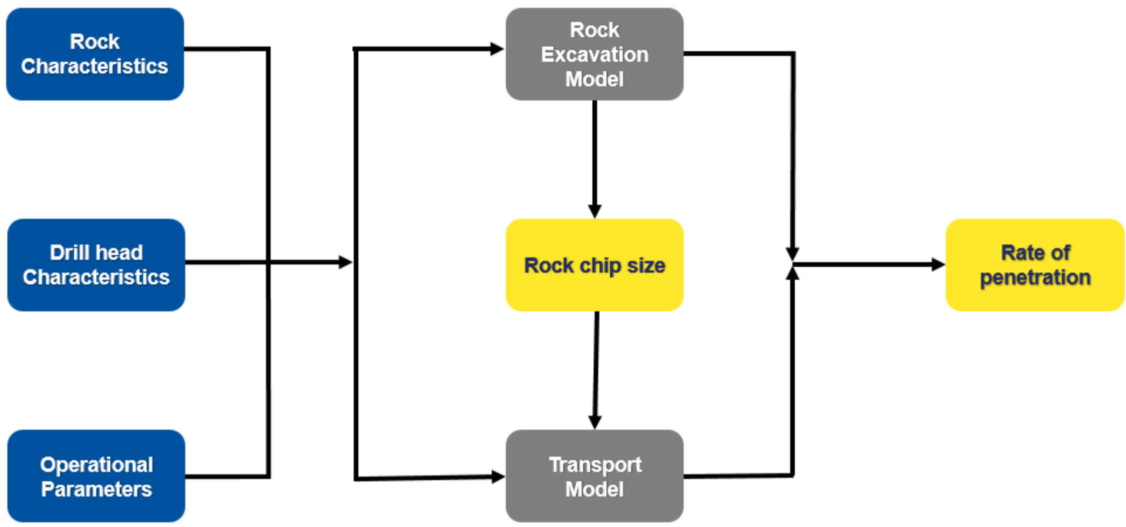

Figure 4.1: Flowchart of the drilling model.

4.2 Rock excavation model

The rock excavation model has been developed to calculate the rate of penetration for four different types of tools: pick points, tooth bits, button bits and v-shaped disc bits.

Assumptions

In order to use the rock excavation theory, the model consists of the following assumptions which will be explained below:

- The rock is homogeneous.
- The applied thrust is the sum of the normal forces on each tool.
- The applied torque is the sum of the individual tangential forces multiplied with their lever arm.
- The excavation depth remains constant with the increase of the rotational speed of the drill.
- All the excavation tools have the same penetration depth.
- Inertia effects are neglected.

Rock cutting theory is only validated against homogeneous rocks; therefore, it is not possible to incorporate the inhomogeneous behaviour of rocks.

According to Mellor (1980), the applied thrust can be calculated by the summation of the individual normal forces. Respectively, the amount of torque can be calculated by the sum of the individual tangential force on each tool multiplied by their individual lever arm. This approximation is only valid when the drill follows a shallow helical penetration path, which is the case during drilling large diameter holes.

Not a clear relationship between the influence of the rotational speed versus the excavation depth has been found in literature. Therefore, the excavation depth is assumed constant with increasing rotational speed. As a result, the drilling rate scales in proportion to the rotational speed.

For simplicity the drill head is taken as a flat surface which results in the same penetration depth for all the excavation tools located underneath the drill head.

The rotational speed of the drill is in the order of 8 rpm. Inertia effects are therefore neglected in the model.

4.2.1 Calculation steps excavation model

Every drill head, regardless of the excavation mechanism follows the same calculation procedure as shown in Figure 4.2.

Figure 4.2: Flowchart rock excavation model.

1. Define the input parameters based on the type of drill head and cutting mechanism to calculate the drill rate. The input parameters are separated into rock characteristics, drill characteristics and operational parameters.

2. Calculate for every depth the normal and tangential force for every UCS value between 0-100 MPa. The applied thrust equals the summation of the individual normal forces. Respectively the amount of torque is equal to the sum of the individual tangential force on each tool multiplied by the individual cutter radius.

3. Check for every depth and UCS value, if the calculated torque or thrust is lower than the operating torque or thrust. When one of the calculated values equals the operating condition, the maximum obtainable excavation depth is reached.

4. With to the excavation depth, rock characteristics and geometry of the cutting tool, the excavated volume can be determined.

5. The rate of penetration is determined by dividing the production of the drill per hour with the area of the pile. The production follows from the excavated volume and rotational speed of the drill.

4.2.2 Calculation procedure pick points

Step 1 - Input parameters

The excavation model needs the following input parameters (see Table (4.1)) to calculate the rate of penetration for pick points.

Table 4.1: Input parameters for the rock excavation model.

Type	Parameter	Symbol	Unit
Rock characteristics	Unconfined Compressive Strength	σ_c	[MPa]
	Brazilian Tensile Strength	σ_t	[MPa]
	Internal friction angle	δ	[°]
Drill head characteristics	Diameter pile	D_{pile}	[m]
	Number pick points	nr_{picks}	[−]
	Tip angle	α	[°]
	Rake angle	β	[°]
Operational characteristics	Thrust	P	[kN]
	Torque	T	[kNm]
	Rotational speed	ω_r	[rpm]

Step 2 - Torque and thrust

The total required torque equals the summation of the individual cutting force multiplied with its lever arm. The cutting forces are calculated with the theory of Li et al. (2018) from Equation 3.26, which is corrected for the mean cutting force by dividing it with a factor 2.25. Normally, the picks points are equally spread over the diameter of the drill, which leads to an average lever arm of $0.25D_{pile}$ resulting in the following formula for the required torque:

$$T = 0.25 D_{pile} nr_{picks} \frac{\lambda_{Li}^{\frac{5}{6}} K_{Ic} d^{\frac{5}{3}}}{6.75 \sqrt[6]{\frac{\pi^2}{12\cos(\beta)} \left[\frac{1}{3} \left(\frac{\sin(\alpha)}{\cos(\beta)} - 1 \right)^2 + 1 \right]}} \tag{4.1}$$

Where T is the amount of torque required to rotate the drill and nr_{picks} is the number of pick points on the drill.

The amount of thrust equals the individual normal forces multiplied with the amount of pick points. Not a clear relation was found by Li et al. (2018) for calculating the normal forces on a pick point. Therefore, the model uses the empirical relation between the normal force and penetration depth (Equation 3.33) obtained by Bilgin et al. (2006). The required thrust for every depth becomes:

$$P = nr_{picks} \cdot 0.752 \cdot \sigma_c^{1.051} \cdot d \tag{4.2}$$

Where P equals the amount of thrust.

Step 3 - Excavation depth

The drill can be either torque or thrust limited. When one of the calculated torque or thrust values equals the operational torque or thrust values, the maximum obtainable excavation depth is reached. The torque limit needs to be avoided, because exceeding this limit results in the drill to stall. The thrust limit only limits the penetration rate, but does not influence the operability of the drill.

Step 4 - Excavation volume

The excavation area depends on the cutting depth in combination with the breakout angle of the pick point. The angle is assumed to be equivalent to the breakout angle defined by Paul and Sikarskie (1965):

$$\psi = \frac{1}{2}[(\frac{\pi}{2}) - (\frac{\alpha + \varphi}{2})] \tag{4.3}$$

Where ψ is the breakout angle as shown in Figure 4.3). The excavation area per pick point is obtained by:

$$A_{picks} = \tan(90^\circ - \psi)d^2 \tag{4.4}$$

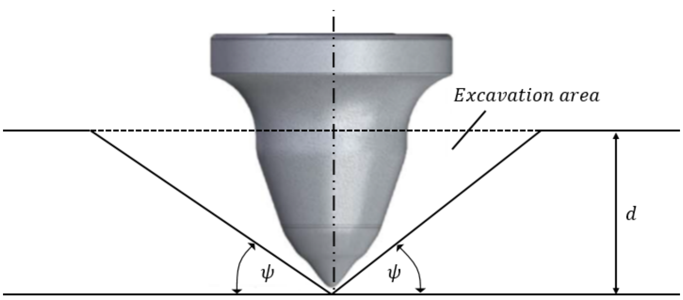

Figure 4.3: Excavation area per pick point.

So far, only one pick point is considered for determining the excavation area. However, when multiple picks are located next to each other, they can interact with each other. For every cutting depth there is an optimal spacing between the pick points which requires a minimum amount of energy (Figure 4.4).

According to Evans (1984), the optimum spacing is determined by the following relation:

$$s = 2d\sqrt{3} \tag{4.5}$$

Where s is the spacing between the pick points.

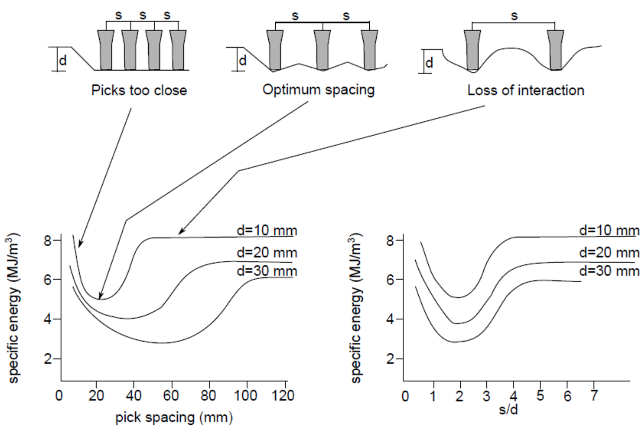

Figure 4.4: Effect of pick spacing on specific energy (Roxborough and Sen, 1986).

To determine the total excavation area, three options are distinguished to incorporate the effect of spacing:

1. **The picks do not interact with each other.**
   The excavation area equals the amount of pick points multiplied with the area obtained from every individual pick point:

$$A_{picks} = nr_{picks}\tan(90^\circ - \psi)d^2 \tag{4.6}$$

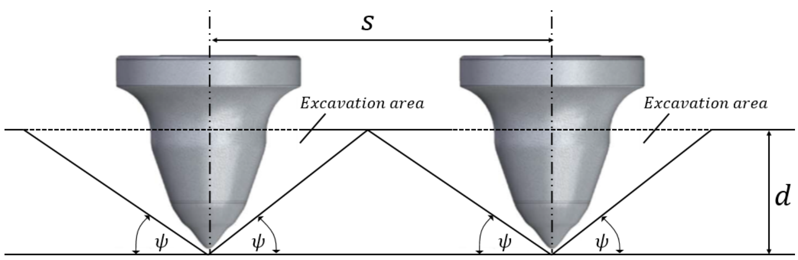

Figure 4.5: Excavation area of two pick points without interaction.

2. **The picks interact with each other**
   According to Equation 4.5, interaction between the picks occurs when the spacing equals $2\sqrt{3}d$. Assuming an break out angle of 30°, the pick points interact with each other at the moment the excavation areas start to overlap each other. To incorporate this effect in the model, the overlap area is assumed to be excavated as an extra region below the existing area as is shown in Figure 4.6. Also a reduction in force due to the interaction between the cracks is noticeable, which leads to a decrease in specific energy. It is not possible to incorporate this effect theoretically and is therefore not implemented in the model as a conservative approach. Furthermore, it has to be noted that the excavated area including the overlap area can never exceeds the area that equals the cutting depth multiplied with the radius of the drill:

$$A_{picks} = nr_{picks}\tan(90^\circ - \psi)d^2 \leq 0.5D_{pile}d \tag{4.7}$$

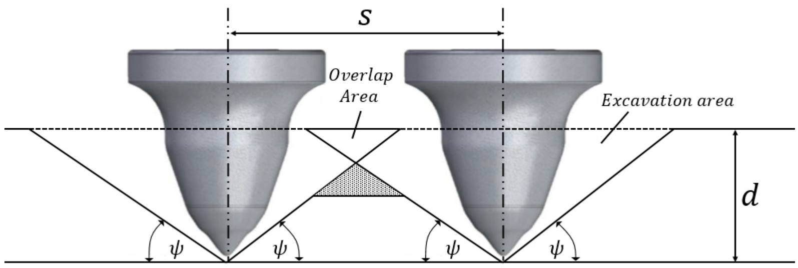

Figure 4.6: Pick points that interact and overlap each other.

3. **The picks are too close to one another.**
   If the picks are too close to one another (Figure 4.7), the drilling is not optimal. More specific energy is required to excavate the same amount of rock compared to an ideal relieved cutting condition. Also, the use of more pick points leads to a lower normal force and thereby smaller excavation depth per pick point. The excavation area is equivalent to the full width of the drill multiplied with the radius:

$$A_{picks} = 0.5 D_{pile} d \tag{4.8}$$

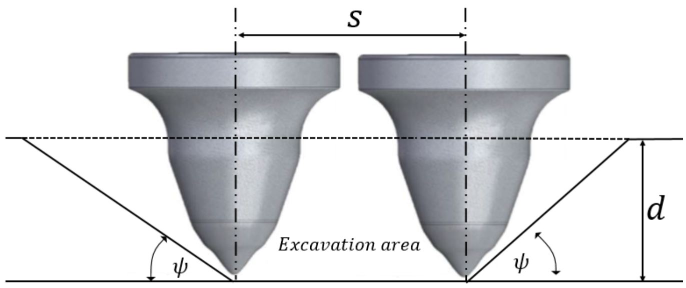

Figure 4.7: Pick points that are too close to one another.

Now the total excavation volume equals the excavation area multiplied with the covered distance per round. Assuming that the picks are equally spread over the diameter, the average covered distance for a pick point equals the circumference at half the radius of the drill head and the excavated volume per round becomes:

$$V_{picks} = 0.5\pi D_{pile} A_{picks} \tag{4.9}$$

Step 5 - Rate of penetration

Calculate the rate of penetration by dividing the production of the drill with the area of the pile:

$$ROP = \frac{Q_{picks}}{0.25\pi D_{pile}^2} \tag{4.10}$$

Where the production of the pick points Q_{picks} equals the excavation volume per hour of the drill:

$$Q_{picks} = V_{picks} \cdot \omega_{r.drill} \cdot 60 \tag{4.11}$$

4.2.3 Calculation procedure toothed cutters

Step 1 - Input parameters

The excavation model needs the following input parameters (see Table 4.2) to calculate the rate of penetration for toothed cutters:

Table 4.2: Input parameters for the rock excavation model.

Type	Parameter	Symbol	Unit
Rock characteristics	Unconfined Compressive Strength	σ_c	[MPa]
	Internal friction angle	δ	[°]
Drill head characteristics	Diameter pile	D_{pile}	[m]
	Number of roller bits	nr_{bits}	[−]
	radius roller bit	r_{bit}	[m]
	Number of teeth per bit	nr_{teeth}	[−]
	Tooth width	w_{teeth}	[m]
	Tip angle	α	[°]
Operational characteristics	Thrust	P	[kN]
	Torque	T	[kNm]
	Rotational speed	ω_r	[rpm]

Step 2 - Torque and thrust

Calculate, for every depth and every UCS value between 0-100 MPa, the normal and rolling force on each bit. The normal force depends on the penetration depth of the bit, the number of teeth entering the rock and the geometry of the teeth. A tooth bit exists of three rollers that are slightly rotated to each other as shown in Figure 4.8 and schematically represented in Figure 4.9. It is necessary to determine the number of teeth entering the rock at every cutting depth. Thereafter, the total bearing surface of the tooth bit is equivalent to the sum of the individual tooth bearing surfaces, where the individual bearing surface equals:

$$A_{tooth} = 2d\tan(\alpha)w_{teeth} \tag{4.12}$$

Figure 4.8: Roller bit with teeth (tooth cutter)(roc).

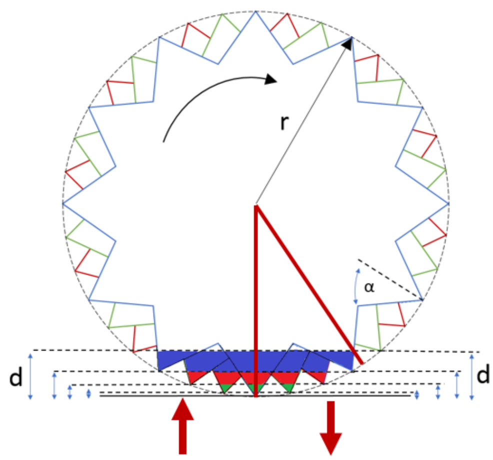

Figure 4.9: Schematically representation of a tooth cutter.

During the excavation process, a tooth penetrates the rock surface until it reaches the maximum excavation depth. From that point, the penetration depth decreases till the moment the tooth leaves the rock. To calculate the effective bearing surface of one tooth bit, the area is taken as half of the total bearing surface area obtained by the summation of the individual teeth, assuming that only the penetrating phase of teeth transfer forces into the rock. According to Equation 3.55 obtained from Wijk (1992), the normal force on a roller bit becomes:

$$F_N = 3 \cdot \sigma_c \frac{A_{bit}}{2} \tag{4.13}$$

Where A_{bit} equals the summation of the individual bearing surfaces of the teeth entering the rock. The total required thrust equals the penetration force per bit multiplied with the number of bits:

$$P = 1.5 \cdot nr_{bits} \cdot \sigma_c A_{bit} \tag{4.14}$$

The required torque equals the sum of the rolling force of each bit multiplied with their lever arm. There are more bits located at the outer radius of the drill than at the centre. Assuming that the average lever arm of the bits is located at $\frac{2}{3}$ of the radius, the required torque, including the theory of Warren et al. (1984) given in Equation 3.56, becomes:

$$T = \frac{1}{3} D_{pile} \cdot nr_{bits} \cdot F_N \frac{\sqrt{2r_{bit}d - d^2}}{r_{bit} - d} \tag{4.15}$$

Step 3 - Excavation depth

Check if the calculated torque and thrust values are lower than the operating torque and thrust values. When one of the calculated values equals the operating condition, the maximum obtainable excavation depth is reached. The excavation depth can be limited by either torque or thrust. The minimum depth determines the excavation depth of the pick point. The torque limit needs to be avoided, because exceeding this limit results in the drill to stall. The thrust limit only limits the penetration rate, but does not influence the operability of the drill.

Step 4 - Excavation volume

Calculate the excavation volume by taking the cutting depth in combination with the breakout angle and the width of the tooth. The breakout angle is taken equivalent to the breakout angle defined by Paul and Sikarskie (1965):

$$\psi = \frac{1}{2}\left[\left(\frac{\pi}{2}\right) - \left(\frac{\alpha + \varphi}{2}\right)\right] \tag{4.16}$$

The excavation volume per tooth is obtained by:

$$V_{tooth} = d^2 \tan(90^\circ - \psi) w \tag{4.17}$$

To obtain the total excavation volume of the drill, first the total amount of teeth entering the surface have to be known. The number of teeth entering the surface depends on the rotational speed of each bit, the distance from the centre and the a number of teeth on each bit (nr_{teeth}). The drill bits are spread over the drill head equally, which results in more drill bits at the outer radius of the drill than in the centre. Assuming that the bits have an average distance of $\frac{2}{3}$ times the radius of the pile, the covered distance per round equals:

$$s_{bit} = \frac{2}{3} \pi D_{pile} \tag{4.18}$$

The average amount of rotations per bit for each round is determined by:

$$\omega_{r.bit} = \frac{2\pi D_{pile}}{6\pi r_{bit}} = \frac{D_{pile}}{3r_{bit}} \tag{4.19}$$

Where r_{bit} is the radius of the drill bit. The total amount of teeth entering the rock in one rotation of the drill are :

$$nr_{indent} = \frac{D_{pile}}{3r_{bit}} \cdot nr_{bits} \cdot nr_{teeth} \tag{4.20}$$

Where nr_{indent} is the number of indentations in one round, nr_{bits} are the number of roller bits on the drill and nr_{teeth} are the number of teeth on one roller. Now calculate the excavation volume by multiplying the number of teeth with the excavation volume per tooth:

$$V_{teeth} = nr_{teeth} \cdot V_{tooth} \tag{4.21}$$

Step 5 - Rate of penetration

Calculate the rate of penetration [m/h] by dividing the production of the drill by the area of the pile:

$$ROP = \frac{Q_{teeth}}{0.25\pi D_{pile}^2} \tag{4.22}$$

Where the production of the tooth bits Q_{teeth} equals the excavation volume during one rotation multiplied with the number of revolutions per hour of the drill:

$$Q_{teeth} = V_{teeth} \cdot \omega_{r.drill} \cdot 60 \tag{4.23}$$

4.2.4 Calculation procedure button and v-shaped disc cutters

The calculation procedure for button and v-shaped disc cutters is similar to procedure of the toothed cutters. Although, there are some differences which are highlighted in this section.

The individual bearing surface changes with geometry and can be calculated for v-shaped discs with the following equation:

$$A_{disc} = 4d\tan(\alpha)\sqrt{2rd - d^2} \tag{4.24}$$

For a button shaped indenter, the equation becomes:

$$A_{button} = \pi(r_{button}^2 - (r_{button} - d)^2) \tag{4.25}$$

Where r_{button} equals the radius of a button.

For calculating the required torque, the theory of Home et al. (1978), explained in section 3.3.3, is included for button cutters and results in the following equation:

$$T = \frac{1}{3}D_{pile} \cdot nr_{bits} \cdot fP \tag{4.26}$$

Furthermore, button and v-shaped disc cutters are mainly used for excavation of hard abrasive rocks. Therefore, for simplicity, the model assumes that the excavation is dominated by the formation of cracks between the indenters. The volume of rock removed per round equals a layer with a thickness equivalent to the indentation depth.

4.3 Transport Model

The rock chips generated by the excavation process, need to be transported to continue the drilling process. In most cases transportation of cuttings takes place using an airlift system (Section 2.4). At large drilling rates, the airlift system can limit the rate of penetration when the excavation process is faster than the transportation process.

In order to determine the transport limit, the drilling model incorporates an airlift model based on Schulte (2013). The transport model uses the momentum balance to solve the relation between the liquid, solid and gas quantities. Schulte (2013) adapted the model of Yoshinaga and Sato (1996) and combined it with the hindered settling theory of Van Rhee (2018). The model makes a distinction between a lower part that consists of a two-phase water-solid flow and an upper part with a three-phase water-solid-gas mixture flow, incorporating the following assumptions:

- Steady-state, there is no variation over time
- One dimensional, only the variation in z-direction is taken into account.
- No temperature variation within the riser.
- The liquid and solids are incompressible.
- The particles are uniform in shape, size and density.
- The particles are transported by the liquid.

In order to determine the transport limit, the model solves the momentum balance which consists of 7 terms added together:

$$\begin{aligned} &\underbrace{A_r\{j_l\rho_l v_{l,E} + j_s\rho_s v_{s,E}\}}_{G_1} - \underbrace{A_r\{j_{g,O}\rho_{g,O}v_{g,O} + j_l\rho_l v_{l,O} + j_s\rho_s v_{s,O}\}}_{G_2} \\ &+ \underbrace{A_r\{\Delta p_2 + \Delta p_E\}}_{G_3} + \underbrace{A_r\{\int_I^O p_3(z)dz + \Delta p_I\}}_{G_4} - \underbrace{A_r g L_{EI}\{\rho_L C_{L,2} + \rho_s C_{S,2}\}}_{G_5} \\ &\underbrace{- A_r g \int_I^O \{\rho_G(z)C_G(z) + \rho_L C_{L,3}(z) + \rho_S C_{S,3}(z)\}dz}_{G_6} + \underbrace{A_r\{\rho_L g(L_{EI} + L_{IA})\}}_{G_7} = 0 \end{aligned} \tag{4.27}$$

- G_1 and G_2 are respectively the in- and outflow terms.
- G_3 and G_4 are the friction losses in the two-phase and three-phase flow.
- G_5 and G_6 are the terms for the two-phase and three-phase flow that take the weight of the mixture into account
- G_7 includes the hydrostatic pressure influence surrounding the suction pipe.

Where A_r is the cross sectional area of the riser, j is the volumetric flux, ρ is the density and v is the velocity, where the subscripts represent the liquid l, solids s and gas g phase.

The letters in the equations are the location in the suction pipe. E is the entrance of the pipe, I is the injection location for the air, A is the surface of the water level and O is the outlet of the airlift pipe as shown in figure 4.10.

In the third and fourth term, Δp_2 is the wall friction loss in lower section of the riser and Δp_3 in the upper section, Δp_E is inlet loss at the entrance and ΔP_I is the loss due to the injection of the air. λ is friction factor. ξ_E and ξ_a are the friction coefficients due to inlet losses (0.56) and acceleration losses (1) which are defined by Yoshinaga and Sato (1996). q_2 and q_3 are the dynamic pressure losses for the lower and upper section, respectively $C_{L.2}$ and $C_{S.2}$ are the steady concentration of the liquid and solids in the two-phase flow and $C_{G.3}$ $C_{L.3}$ and $C_{S.3}$ are the varying gas, liquid and solids concentration over the vertical in the three-phase flow.

The model of Schulte (2013) calculates the solid flux j_s and corresponding liquid flux j_l for a given gas flux j_g using a bisection method. The five different concentrations are determined by iterating volumetric fluxes until the difference between the gas concentration is below 10^{-5}. The calculation procedure is given in Figure 4.11 as a flowchart. The equations derived by Schulte (2013) are added in Appendix C.

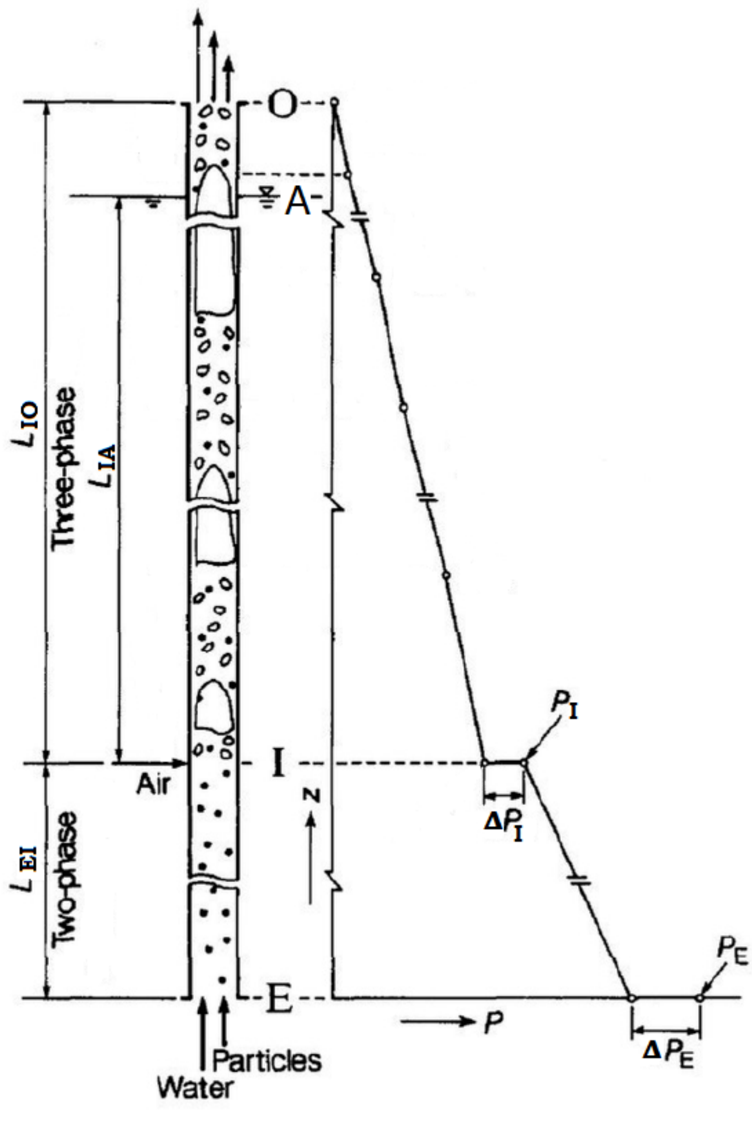

Figure 4.10: Principle of airlift model.

In order to find the transport limit of the airlift system, the model is adopted to find the maximum solid flux that is possible to be transported through the airlift pipe. It increases the solid flux until reaching the point where the momentum equation is unsolvable. At that moment the airlift system is not able to transport the amount of solids to the surface due to the increase in losses within the riser. Furthermore, the following assumptions are added to the model which will be explained below:

- The Darcy friction factor is calculated according to Nikuradse (1950) assuming Re > 100.000:

$$\lambda = \frac{0.25}{\left(log(3.7 \cdot \frac{D_r}{\epsilon_w \cdot 1000})\right)^2} \tag{4.28}$$

  Where ϵ_w is the roughness of the wall and D_r is the diameter of the airlift pipe

- The maximum concentration of solids in water is 0.08%.
- The minimum velocity of water in the lower section of the pipe is above 3 m/s

In the original model λ is taken as a constant.

When there is no maximum concentration limit, the model increases the solid flux to an unrealistic value by lowering the water velocity. An maximum concentration of approximately 8% is found in the experiments of Weber and Dedegil (1976), which is assumed as the transport limit for the airlift system.

If the horizontal inwards velocity over the rock chips towards the suction pipe is lower than the critical velocity to transport the cuttings as bed load, the airlift system is not able to transport the material underneath the drill head which is assumed to be 3 m/s.

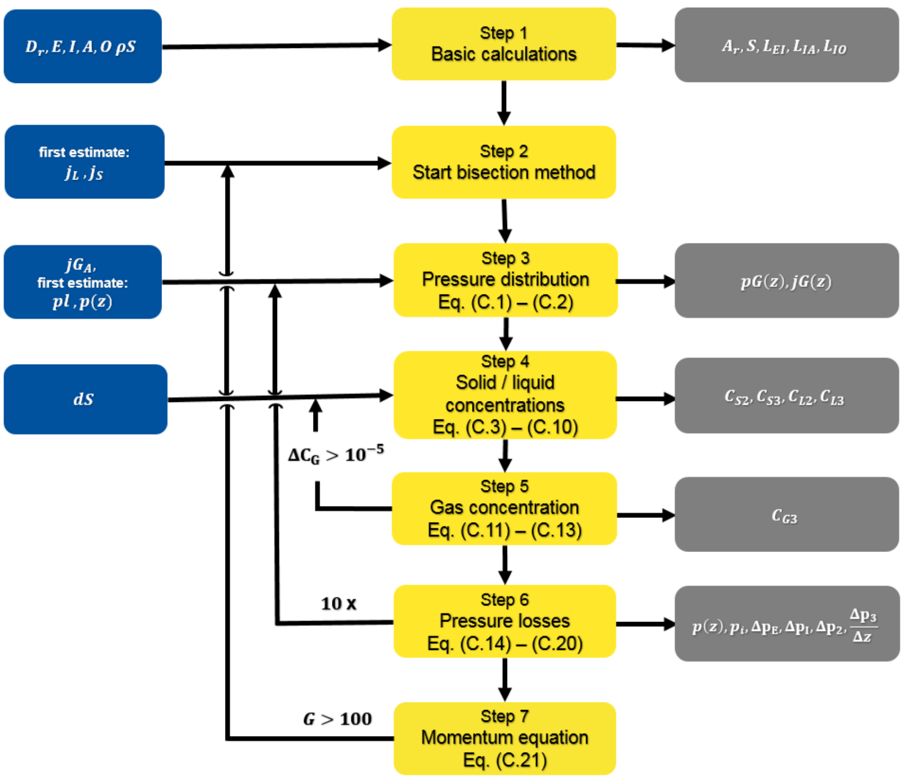

Figure 4.11: Calculation procedure based on Schulte (2013).

5 | Validation of the drilling model

This chapter is divided in two parts. The first part validates the excavation model with experimental data and the second part validates the transport model with a dataset from a full-scale airlift experiment.

5.1 Rock excavation model

Unfortunately, limited data from drilling large diameter piles offshore is available or accessible to validate the excavation model. However, data is available from the onshore raise boring industry, which uses a similar drilling technique. Within this section, drilling data from the Kure Copper Mine (Shaterpour-Mamaghani and Bilgin, 2016) and a tunnel in Olkiluoto (Autio and Kirkkomäki, 1996) is used for validation.

5.1.1 Kure Copper Mine

In the Kure Copper Mine, located in northern part of Turkey, a raise boring machine bored a 22 m long ventilation shaft with a diameter of 2.6 m. The performance of the raise boring machine (RBM) was measured during operation, which is described by Shaterpour-Mamaghani and Bilgin (2016). A general overview of the reamer head is shown in Figure 5.1. At the top of the stem there is a small drill, which drills a pilot hole before the reamer starts enlarging this hole. This is something that is not used in the offshore drilling industry. The RBM used in the operation was able to produce 4159 kN thrust, 210 kNm torque and had a maximum rotational speed of 17 rpm. The cutter head used in the operation contained 16 roller bits, that consist of 129 tungsten carbide inserts each. The drilling operation is discontinuous, which causes the drill to advance one length of a rod at a time. After drilling one length, another rod needs to be added to proceed any further. During the drilling cycle of one drill string, also called drill rod, the mean operating torque and thrust values were measured which are shown in Figure 5.2. The rock UCS value was 81.6 ± 29.3 MPa and the BTS value was 10.96 ± 2.7 MPa. The complete dataset, including the measured values, is given in Appendix D.

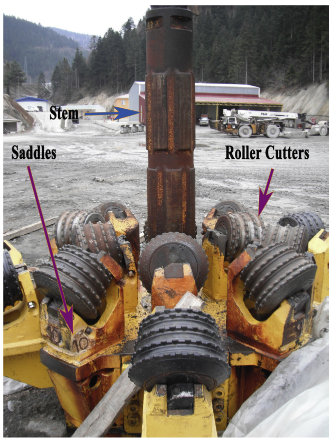

Figure 5.1: Example of a raise boring reamer head Shaterpour-Mamaghani and Bilgin (2016).

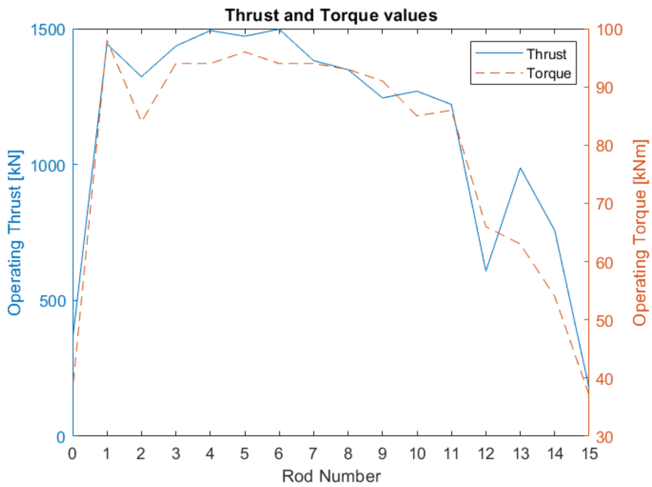

Figure 5.2: Measured thrust and torque values Kure Copper Mine.

The rate of penetration obtained with the excavation model is compared to the measured values of the mine (Figure 5.3). The blue dashed line shows the measured rate of penetration and the red line shows the simulated value. The grey area corresponds with the variation in UCS value, with an upper bound of 110 MPa and a lower bound of 52 MPa. It is clearly visible that the excavation model underestimates the rate of penetration for the first rod and for the last four rods. Shaterpour-Mamaghani and Bilgin (2016) noted that the first measurement (rod 0) equals the rate of penetration of the small reamer and can therefore be neglected. They also stated that the drilling performance during the last three rods (13, 14 and 15) is exceptional. The operator gradually decreases the operational values of the drill (Figure 5.2) to lower the drilling rate and prevent the hole from collapsing, but the rate of penetration stayed more or less constant. They presumed this phenomena occurred due to the inhomogeneity of the rock, which is not incorporated in the drilling model.

In the middle part between rod number 1 and 12, the model shows good a good fit with the values obtained from the validation data. Differences between the model and the measured values can be related to a difference in UCS value.

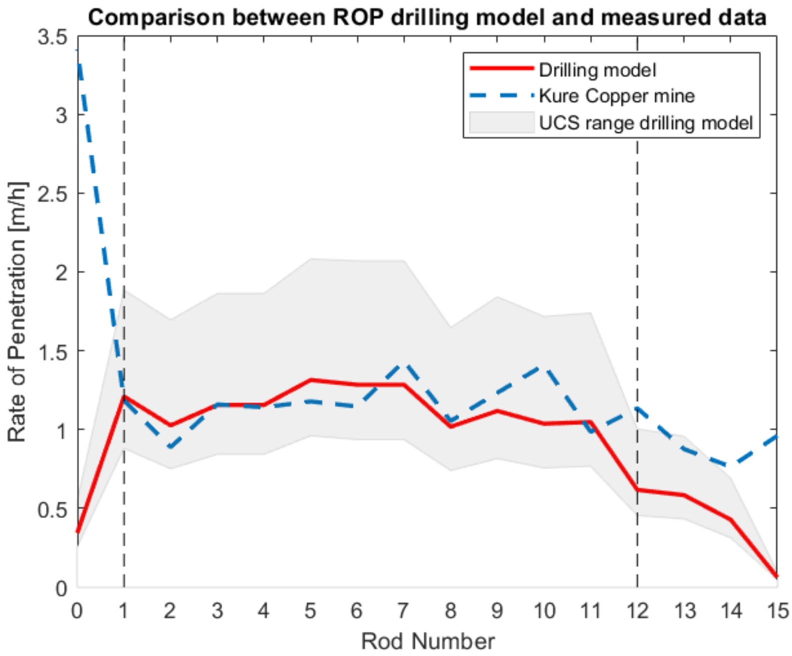

Figure 5.3: Drilling rates experiments vs drilling model.

5.1.2 Olkiluoto

For the waste disposal of the Olkiluoto nuclear power-plant, located at the south-west coast of Finland, three full-scale deposition holes were bored at a depth of 60 m. The operation took place in 1992 with a raise boring machine as is shown in Figure 5.1. The deposition holes were 1.5 m in diameter and 7.5 m in depth. During the operation, one of the main objectives, described by Autio and Kirkkomäki (1996), was to:

"provide information about the performance of the boring machine and in particular about the parameters which govern boring performance so that the costs of using the method can be estimated."

In order to determine the effect of the operating parameters on the drilling rate, several tests were carried out by varying the amount of thrust and rotational speed for two different cutter head configurations, which is given in Appendix D. The hole consisted of rock with an UCS value of approximately 75 MPa and the BTS value of 9 MPa. The RBM used in the operation was able to produce 630 kN thrust, 74 kNm torque and had a maximum rotational speed of 12 rpm. The cutter head was equipped with 8 roller cutters underneath the drill head that consist of button inserts (Figure D.1). A combination of 5- and 6-row bits with a total of 44 rows were used in for excavating the second hole and a combination of 4- and 5-row bits with a total of 36 rows were used in the third hole. The corresponding numbers of grooves on the bottom of the hole were respectively 30 and 24, because some of the buttons followed the same groove. The total number of buttons per row was not specified but is estimated to be 30.

Comparing the results of the excavation model with the experiments shows a good match between the predicted and measured value. However, for the lower drilling rates the model slightly overestimate the measured drilling rate and at larger drilling rates the model tends to underestimate the drilling rate. This difference can be explained due to a difference in geometry of the indenters. The indenters used the model were assumed as spheres, while in reality the bearing surface of the indenter was more flattened at the top and increases less over depth compared to a spherical indenter. This difference in geometry ensures a larger bearing surface for smaller excavation depths which leads to a lower ROP and a smaller bearing surface at larger penetration depths, which results in an increase in ROP.

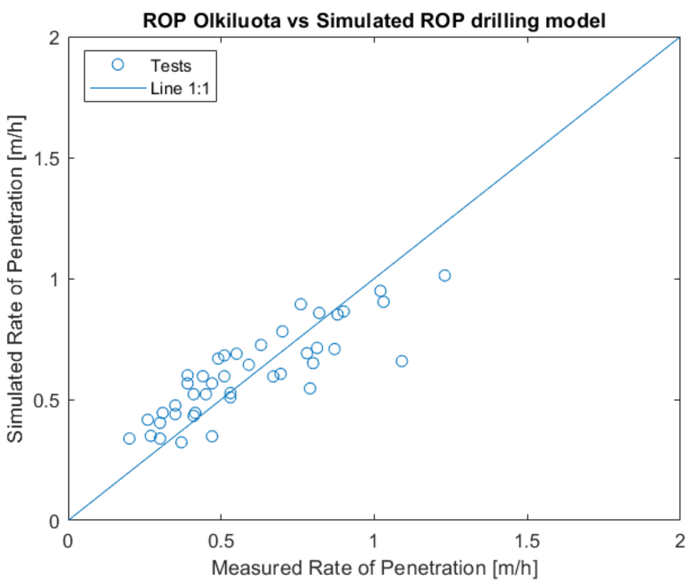

Figure 5.4: Validation excavation model.

5.1.3 Case study

According to the experiments described in the previous sections, the model calculates the drilling rate reasonably well. However, for all the experiments, the operational parameters, rock and drill head characteristics were already known. To predict the rate of penetration for an upcoming drilling project it is not that straightforward. The UCS value depends on the preliminary investigation, which can easily have an uncertainty of 50% for different layers. Specific drill head characteristics such as the number, type and location of the bits are rarely supplied by drilling contractors. The maximum amount of thrust, torque and rpm are known, but the operational conditions are still uncertain.

To see the influence of the operational conditions on a large diameter drill, a large diameter drill is simulated and compared with experimental data obtained from a drilling manufacturer. The drill consists of 30 pick points, 350 kN thrust capacity, 275 kNm torque and has a rotational speed of approximately 8 rpm. The drill head has a diameter of 2.3 m and consist of 30 pick points. The drill does not use an airlift system, but the rock cuttings are removed by a centrifugal pump. The transport capacity of solids of the centrifugal pump is approximated to be 21 m^3/h, which limits the rate of penetration at 5 m/s. The results of the drilling model are represented in Figure 5.5 and field data is shown as dots for different materials.

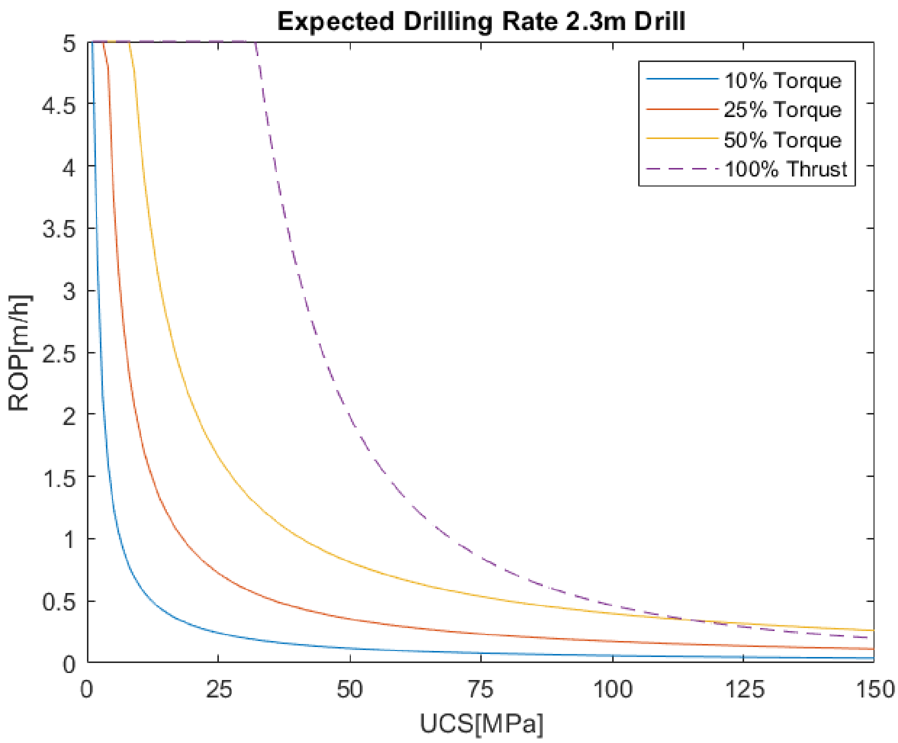

Figure 5.5: Comparison of the drilling model for different operational torque values with field data for a 2.3 diameter drill.

It can be concluded that the model overestimates the drilling rate for hard clay layers. The drilling rate for sand and gravel is assumed to be limited by the centrifugal pump. A good relation is found between 20 - 30% of the maximum torque. A similar observation was found by Vantomme et al. (2017), who predicted the rate of penetration for a large diameter drill with a diameter of 4.25 m and found matching values operating at 20% of the maximum torque capacity.

5.2 Transport model

The transport model uses the momentum balance to solve the relation between the liquid, solid and gas quantities. To validate if the model calculates the solid flux correctly, the simulated values are compared with experimental data. Weber and Dedegil (1976) carried out large scale experiments for an airlift system with similar dimensions used by large diameter drills offshore. In the experiment, the riser had a diameter of 300 mm and varied in length between 50 and 450 m. They measured the air-supply, inflow concentration and the outflow volume of solids and water which are given in Appendix C. In the original paper of Weber and Dedegil (1976), a couple of misprints were found for experiments with number 20 till 23. The correct results were given by Weber (1982) and corrected in the Appendix. The maximum delivered volumetric concentration of solids was 8.6% and the air supply varied between 13.2 and 42.8 m^3/min. Two materials which can be found during drilling were used in the experiment with the following characteristics:

- Gravel, $\rho_s = 2575$ kg/m^3, $d_s = 5$ mm
- Sand, $\rho_s = 2610$ kg/m^3, $d_s = 0.5$ mm

The results of the transport model compared to the data obtained from the experiments is shown in Figure 5.6. A reasonably good agreement with the experimental values is found for gravel. Only for one point (experiment number 3), the model overestimated the amount solid flux with almost 100% and is assumed as an error in the measurements. In the case of sand, the model overestimates the solid flux with approximately 20%.

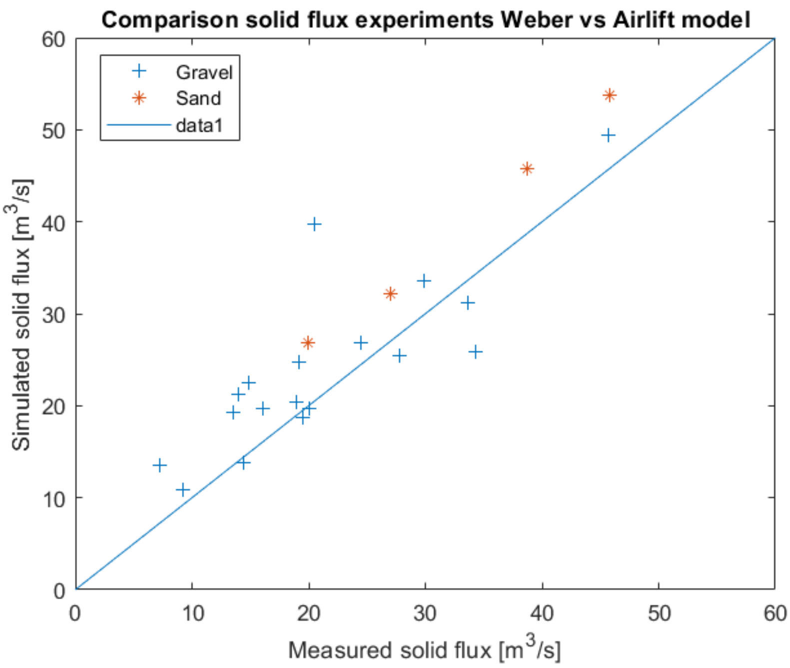

Figure 5.6: Validation airlift model.

Furthermore, the influence of the water depth on the transport limit for calculating the drilling rate is simulated for different pile diameters varying from 2 to 3.5 m (Figure 5.7). Typical values of the airlift system of a top drill were used in the simulation. The riser had a diameter of 300 mm and the air-supply volume was 25m^3/min (atmospheric pressure). The material was taken as gravel with a diameter of 5 mm and a density of 2575 kg/m^3. The inlet point of the air is assumed 1 m above the drill head and the outlet is assumed 10 m above the water surface. It is clearly visible that at shallow water depths the airlift system is not able to transport the material upwards due to an insufficient pressure difference given by the airlift system. At around 20 m water depth, the transport capacity of the airlift system starts increases with depth until it reaches a stable value. A lower transport limit is observed for larger diameters, because a larger volume of rock needs to be transported to maintain the same drilling rate. Often, the airlift configurations do not change with increasing pile diameter, which leads to a lower drilling rate.

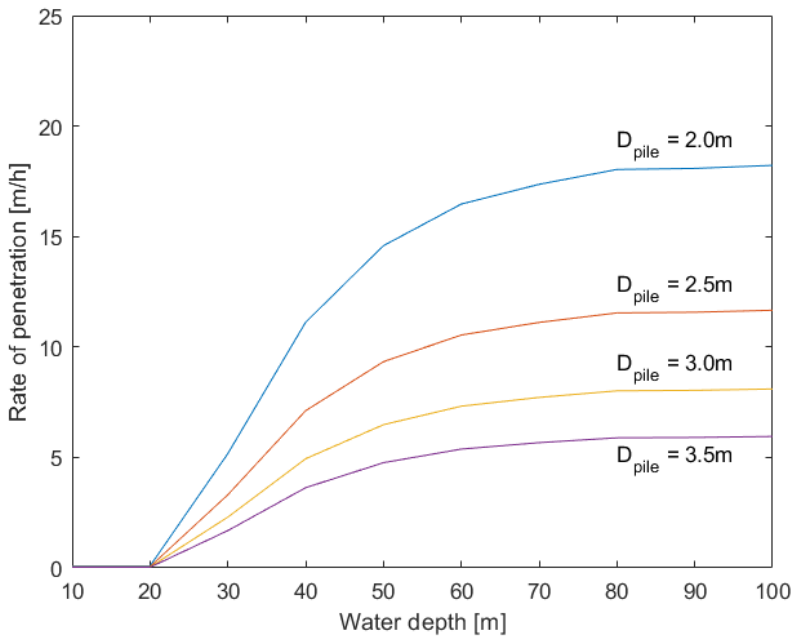

Figure 5.7: Transport limit of four different top drills over depth.

It can be concluded from the graph that installing piles in shallow water depths, the performance of the airlift system decreases for more shallow water depths. For water depths below 20 m, the airlift system is not able to transport the cuttings 10 m above the water surface. Looking at larger water depths the transport limit does not vary anymore. Also, for small diameter drills the transport model does not seems to limit the drilling rate at large water depths, but with increasing pile diameter, the maximum obtainable drilling rate decreases significantly.

6 | Conclusions & Recommendations

A number of conclusions can be made regarding the literature study and the drilling model:

- A theoretical based drilling model is developed that can predict the rate of penetration for different drilling techniques. The model determines the drilling rate based on the excavation and transportation limit. The model is validated with experimental data, which shows a good resemblance with the excavation process from the onshore raise boring industry.
- The drilling model overestimates the drilling rate of hard clays and ductile rock. They are hard to excavate, because the formation of cracks is limited. In these cases, the use of pick points is preferred above indentation tools.
- The transportation is limited by the maximum amount of cuttings that can be transported through an airlift system. Simulations have shown that at small water depths, the drill is not able to transport the cuttings upwards. Depending on the configuration, the airlift system is effective at a critical depth from where the performance of the system improves for increasing water depth. At large water depths, the airlift system tends to a constant value.
- Looking at the existing drills, the geometry of the airlift system does not increase in proportion with the diameter of a drill. As a result, transportation of cuttings will limit the drilling rate sooner for larger diameters.

The following recommendations can be made for further study or research:

- This thesis focuses on the drilling rate of the pile installation. For estimating the total required time for the pile installation in tender phase, other operations need to be taken into account such as the preparation of the drill, grouting of the pile, transportation of the vessel and delay due to weather conditions.
- A very limited amount of validation data for drilling offshore foundation piles is found for the operational conditions which have a large influence on the drilling rate. More data needs to be collected to validate the model further and get a more reliable prediction of the drilling rate.
- In order to transport the cuttings through the airlift system, the cuttings need to be transported underneath the drill head to the suction hole. This transport of cuttings is assumed not to be the limiting factor of the drilling process but should be investigated further to be sure that it does not limit the drilling rate.
- The drilling model is based on dry atmospheric rock cutting theory. Saturated effects are not taken into account and the influence of water depth is neglected. However, during the cutting of weak rock, an increase in cutting forces is found in literature. More research towards the cutting behaviour of saturated rock is desired to incorporate the effects within the drilling model.
- The model assumes the rock to be homogeneous. The presence of boulders is not taken into account, which decreases the drilling rate. More field data is needed to determine the influence of boulders on the drilling rate.

Bibliography

Dth reverse circulation hammer drilling. http://www.hdengineering.com/applications/dthrc.html. Accessed: 2018-10-10.

Geological france. http://www.statistiques.developpement-durable.gouv.fr/lessentiel/ar/2055/0/patrimoine-geologique-france.html. Accessed: 2018-09-28.

Rockrollercutters. http://www.rock-cutters.com/rcd-roller-cutters/. Accessed: 2018-11-12.

Stds. https://stds.de/portfolio-item/rotary-drilling-tools/?lang=en. Accessed: 2018-11-12.

Wikipedia. https://en.wikipedia.org/wiki/Hjulstr%C3%B6m_curve. Accessed: 2018-11-28.

Autio, J. and Kirkkomäki, T. (1996). Boring of full scale deposition holes using a novel dry blind boring method. Technical report, Swedish Nuclear Fuel and Waste Management Co.

Bauer (2016a). Bauer maritime technologies.

Bauer (2016b). Bauer service katalog.

Bilgin, N., Copur, H., and Balci, C. (2013). *Mechanical excavation in mining and civil industries.* CrC Press.

Bilgin, N., Demircin, M., Copur, H., Balci, C., Tuncdemir, H., and Akcin, N. (2006). Dominant rock properties affecting the performance of conical picks and the comparison of some experimental and theoretical results. *International Journal of Rock Mechanics and Mining Sciences*, 43(1):139–156.

Copur, C. et al. (2003). A set of indices based on indentation tests for assessment of rock cutting performance and rock properties. *Journal of The Southern African Institute of Mining and Metallurgy*, 103(9):589–599.

Evans, I. (1964). The force required to cut coal with blunt wedges. In *International Journal of Rock Mechanics and Mining Sciences & Geomechanics Abstracts*, volume 2, pages 1–12. Elsevier.

Evans, I. (1984). A theory of the cutting force for point-attack picks. *International Journal of Mining Engineering*, 2(1):63–71.

Evans, I. and Pomeroy, C. (1966). *The strength, fracture and workability of coal.* Pergamon.

GmbH, B. M. (2012). "latest developments in hard rock drilling".

Gokhale, B. V. (2010). *Rotary drilling and blasting in large surface mines.* CRC Press.

Goktan, N. et al. (2005). A semi-empirical approach to cutting force prediction for point-attach picks. *Journal of the Southern African Institute of Mining and Metallurgy*, 105(4):257–263.

Goktan, R. (1997). A suggested improvement on evans' cutting theory for conical bits.

Griffith, A. A. and Eng, M. (1921). Vi. the phenomena of rupture and flow in solids. *Phil. Trans. R. Soc. Lond. A*, 221(582-593):163–198.

Grima, M. A., Miedema, S., van de Ketterij, R., Yenigül, N., and van Rhee, C. (2015). Effect of high hyperbaric pressure on rock cutting process. *Engineering Geology*, 196:24–36.

Hatamura, Y. and Chijiiwa, K. (1975). Analysis of the mechanism of soil: 1st report. cutting patterns of soils. *Bulletin of JSME*, 18(120):619–626.

Helmons, R. (2017). Excavation of hard deposits and rocks: On the cutting of saturated rock.

Helmons, R., Miedema, S., Grima, M. A., and van Rhee, C. (2016a). Modeling fluid pressure effects when cutting saturated rock. *Engineering Geology*, 211:50–60.

Helmons, R., Miedema, S., and van Rhee, C. (2016b). Discrete element modeling of circular rock cutting with evaluation of pore pressure effects. *WODCON XXI: Innovations in dredging*.

Home, L. et al. (1978). Limiting factors on economical use of a raise drill. In *Third Australian Tunnelling Conference: Preprints of Papers*, page 90. Institution of Engineers, Australia.

Kahraman, S. and Altindag, R. (2004). A brittleness index to estimate fracture toughness. *International Journal of Rock Mechanics and Mining Sciences*, 2(41):343–348.

Koschinski, D. B. S. and Lüdemann, D. B. K. (2013). Entwicklung schallmindernder maßnahmen beim bau von offshore-windenergieanlagen. *Bundesamt für Naturschutz, Nehmten und Hamburg*.

LDD. Ldd large diameter drilling. `https://www.lddrill.com/services/large-diameter-monopile-drilling/`. Accessed: 2018-06-28.

Li, X., Wang, S., Ge, S., Malekian, R., and Li, Z. (2018). A theoretical model for estimating the peak cutting force of conical picks. *Experimental Mechanics*, pages 1–12.

LTD, B. C. C. (2015). Buma reverse circulation drilling rig.

Mellor, M. (1980). Mechanics of cutting and boring. part 5. dynamics and energetics of identation tools. Technical report, Cold regions research and engineering lab Hanover NH.

Merchant, M. E. (1944). Basic mechanics of the metal-cutting process.

Merchant, M. E. (1945a). Mechanics of the metal cutting process. i. orthogonal cutting and a type 2 chip. *Journal of applied physics*, 16(5):267–275.

Merchant, M. E. (1945b). Mechanics of the metal cutting process. ii. plasticity conditions in orthogonal cutting. *Journal of applied physics*, 16(6):318–324.

MHWirth (2016). Cutters and drilling tools.

Miedema, S. A. (1987). Calculation of the cutting forces when cutting water saturated sand. *Doctor thesis, Delft, Netherlands*.

Miedema, S. A. (2014). *The Delft sand, clay and rock cutting model*. IOS Press.

Miller, M. and Sikarskie, D. L. (1968). On the penetration of rock by three-dimensional indentors.

Mishnaevsky, L. (1995). Physical mechanisms of hard rock fragmentation under mechanical loading: a review. In *International Journal of Rock Mechanics and Mining Sciences and Geomechanics Abstracts*, volume 32, page 763. Oxford; New York: Pergamon Press, 1974-c1996.

Nikuradse, J. (1950). *Laws of flow in rough pipes*. National Advisory Committee for Aeronautics Washington.

Nishimatsu, Y. (1972). The mechanics of rock cutting. In *International Journal of Rock Mechanics and Mining Sciences & Geomechanics Abstracts*, volume 9, pages 261–270. Elsevier.

Paul, B. and Sikarskie, D. L. (1965). A preliminary theory of static penetration by a rigid wedge into a brittle material. *Trans. AIME*, 232:372–383.

Rhee, C. (2018). Lecture notes oe44045.

Richard, T., Detournay, E., Drescher, A., Nicodeme, P., Fourmaintraux, D., et al. (1998). The scratch test as a means to measure strength of sedimentary rocks. In *SPE/ISRM Rock Mechanics in Petroleum Engineering*. Society of Petroleum Engineers.

Roxborough, F. F. and Phillips, H. R. (1975). Rock excavation by disc cutter. In *International Journal of Rock Mechanics and Mining Sciences & Geomechanics Abstracts*, volume 12, pages 361–366. Elsevier.

Schulte, S. (2013). Vertical transport methods in deep sea mining.

Seacore, F. (2014). Developments in xl drilling for monopiles/shafts used in the offshore energy sector.

Shaterpour-Mamaghani, A. and Bilgin, N. (2016). Some contributions on the estimation of performance and operational parameters of raise borers–a case study in kure copper mine, turkey. *Tunnelling and Underground Space Technology*, 54:37–48.

Stevens, R. S., Wiltsie, E. A., Turton, T. H., et al. (1982). Evaluating drivability for hard clay, very dense sand, and rock. In *Offshore Technology Conference*. Offshore Technology Conference.

Tuncdemir, H., Bilgin, N., Copur, H., and Balci, C. (2008). Control of rock cutting efficiency by muck size. *International Journal of Rock Mechanics and Mining Sciences*, 2(45):278–288.

Vantomme, F., Kuo, M.-H., Cathie, D., and Denois, T. (2017). Prediction of drilling rates for large diameter monopiles. In *Offshore Site Investigation Geotechnics 8th International Conference Proceeding*, volume 1092, pages 1092–1099. Society for Underwater Technology.

Verhoef, P. N. (1997). Wear of rock cutting tools.

Vlasblom, W. (2007). Cutting of rock. *Lecture Book Dredging Processes*.

Wagner, H. and Schümann, E. (1971). The stamp-load bearing strength of rock an experimental and theoretical investigation. *Rock mechanics*, 3(4):185–207.

Warren, T. et al. (1984). Factors affecting torque for a roller cone bit. *Journal of petroleum technology*, 36(09):1–500.

Weber, M. (1982). Vertical hydraulic conveying of solids by air-lift. *Journal of pipelines*, 3(2).

Weber, M. and Dedegil, Y. (1976). Transport of solids according to the air-lift principle. In *Proc. 4th Int. Conf. on the Hydraulic Transport of Solids in Pipes, 1976*.

Wijk, G. (1989). The stamp test for rock drillability classification. In *International Journal of Rock Mechanics and Mining Sciences & Geomechanics Abstracts*, volume 26, pages 37–44. Elsevier.

Wijk, G. (1991). Rotary drilling prediction. In *International Journal of Rock Mechanics and Mining Sciences & Geomechanics Abstracts*, volume 28, pages 35–42. Elsevier.

Wijk, G. (1992). A model of tunnel boring machine performance. *Geotechnical & Geological Engineering*, 10(1):19–40.

WindEurope (2017). The european offshore wind industry, key trends and statistics 2016. *Wind Europe: Brussels, Belgium*, page 37.

Yoshinaga, T. and Sato, Y. (1996). Performance of an air-lift pump for conveying coarse particles. *International journal of multiphase flow*, 22(2):223–238.

A | Appendix A

Derivation of the linear cutting model according to Li et al. (2018).

During the rock cutting process, the cracks would be initiated at the tip of the pick and propagated to the free surface. This phenomena suggests that the concentrated stress at the tip of the pick exceeded the rock fracture strength or critical stress of crack initiation (Figure A.1a). According to Griffith and Eng (1921), the critical stress is determined by:

$$\sigma_S = \sqrt{\frac{2E\gamma_{li}}{\pi\delta_{li}}} \tag{A.1}$$

Where σ_S is the critical stress of crack initiation, E is the elasticity modulus, δ_{li} is the length of the initiated crack and γ is the rock surface energy density, which is defined as the energy consumed in generating a unit of surface according to:

$$\gamma_{li} = \frac{K_{Ic}^2}{2E} \tag{A.2}$$

Where K_{Ic} is the fracture toughness of the rock, which can be determined by the empirical relation obtained by Kahraman and Altindag (2004):

$$K_{Ic} = 0.11(\frac{\sigma_c\sigma_t}{2})^{0.43} \tag{A.3}$$

Where σ_c is the Unconfined Compressive Strength and σ_t is the Brazilian Tensile Strength. Combining equation A.1 with equation A.2 leads to:

$$\sigma_S = \frac{K_{Ic}}{\sqrt{\pi\delta_{li}}} \tag{A.4}$$

Figure A.1a shows schematically the stress distribution on a conical pick at the moment of the crack initiation. The direction of the stress is perpendicular to the conical surface. The compressive stress at point C (Figure A.1b) in a random horizontal profile (A-A) is calculated by:

$$\sigma(C) = \frac{d-l}{d}\sigma_S \tag{A.5}$$

Where d is the cutting depth and l is the distance between the horizontal profile and the pick tip. For calculating the stress distribution on the pick point, the horizontal profile is simplified to a circle with radius r (Figure A.1b), which is determined by the two semi-axis of the ellipse a and b as shown in Figure A.1a by:

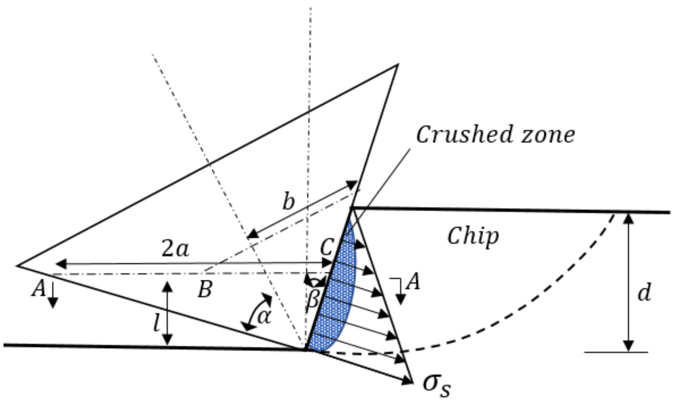

(a) The schematic of stress distribution on the conical pick Li et al. (2018).

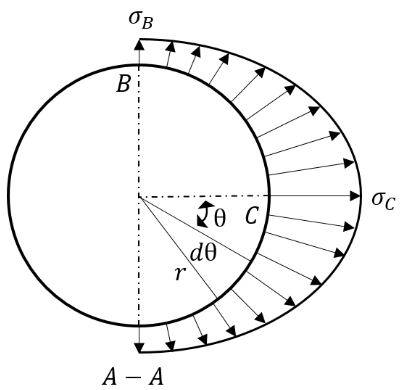

(b) The schematic of stress distribution on the conical pick Li et al. (2018).

$$r = \frac{a+b}{2} = \lambda_{li} l \tag{A.6}$$

The semi-axis a and b can be determined geometrically with:

$$a = \frac{l \tan(2\alpha - \beta) + \tan(\beta)}{2} \tag{A.7}$$

$$b = l \tan(\alpha) \left[\frac{\tan(2\alpha - \beta) - 2\tan(\alpha - \beta) - \tan(\beta)}{2} \sin(\alpha - \beta) + \frac{1}{\cos(\alpha - \beta)} \right] \tag{A.8}$$

Where α is half of the tip angle and β is the rake angle.

Equation A.6 can be rewritten into λ_{li} and l, where λ_{li} only depends on α and β:

$$\lambda_{li} = \frac{\tan(2\alpha - \beta) + \tan(\beta)}{4} + \frac{1}{2} \tan(\alpha) \left[\frac{\tan(2\alpha - \beta) - 2\tan(\alpha - \beta) - \tan(\beta)}{2} \sin(\alpha - \beta) + \frac{1}{\cos(\alpha - \beta)} \right] \tag{A.9}$$

The stress along the circle is assumed to be linear. The stress at a point on the circle is given by:

$$\sigma = k\theta + m \tag{A.10}$$

Where θ is the angle between the point and the cutting direction and k and m are constants. Substituting the central angles and stresses of points B and C of Figure A.1b into Equation A.10 leads to:

$$\begin{aligned} \sigma(C) &= m, \theta = 0 \\ \sigma(B) &= \frac{\pi}{2} k + m, \theta = \frac{\pi}{2} \end{aligned} \tag{A.11}$$

Substituting Equation A.11 into Equation A.10, the stress at a random point on the conical surface of the pick equals:

$$\begin{aligned} \sigma &= \frac{2}{\pi} [\sigma(B) - \sigma(C)]\theta + \sigma(C) \\ &= \left[\frac{2}{\pi} \left(\frac{\sigma(B)}{\sigma(C)} - 1 \right) \theta + 1 \right] \sigma(C) \end{aligned} \tag{A.12}$$

As the pick moves a distance x, the displacement of extruded rock along the direction of the stress (radial displacement) at point B and C are calculated with:

$$\begin{aligned} y(B) &= x \sin(\alpha) \\ y(C) &= x \cos(\beta) \end{aligned} \tag{A.13}$$

Combining Equation A.1, A.5, A.12 and A.13, the stress at a random point can be written as:

$$\sigma = \left[\frac{2}{\pi} \left(\frac{\sin(\alpha)}{\cos(\beta)} - 1 \right) \theta + 1 \right] \frac{(d - l) K_{Ic}}{d \sqrt{\pi \delta_{li}}} \tag{A.14}$$

Li et al. (2018) noted that the stress on the pick is negatively correlated with the size of the crack δ_{li}. They assumed that the stress acting on the pick is largest at the crack initiation and decreases as the crack propagates. They conclude that the peak cutting force occurs when the crack is initiated and decreases as the crack propagates until the chip is separated from the rock. The peak cutting force is calculated by integrating the stress along the surface of the pick point:

$$\begin{aligned} PCF_{This} &= \int_0^d \int_{-\pi/2}^{\pi/2} \left[\frac{2}{\pi} \left(\frac{\sin(\alpha)}{\cos(\beta)} - 1 \right) \theta + 1 \right] \frac{(d-l)K_{Ic}}{d\sqrt{\pi \delta_{li}}} \cos(\theta) \lambda l d\theta dl \\ &= \frac{\lambda_{li} K_{Ic} d^2}{3\sqrt{\pi \delta_{li}}} \end{aligned} \tag{A.15}$$

To calculate the peak cutting force, still the length of the crack has to be known. For calculating δ_{li}, the energy criterion of Griffith's fracture theory is used. It determines the amount of energy needed for creating a crack of a certain length. The work done by the pick or elastic energy stored in the rock should be greater or equal to the energy needed for the crack, which is expressed as:

$$U_0 \geq G_S \tag{A.16}$$

Where U_0 is the work done by the pick point and G_s is the energy needed for generating the new surface during crack propagation according to Griffith and Eng (1921). G_s is determined by a semi-disc with radius δ_{li}, where the surface energy for generating a crack is calculated by:

$$G_S = \pi \delta_{li}^2 \gamma_{li} = \frac{\pi \delta_{li}^2 K_{Ic}^2}{2E} \tag{A.17}$$

The work done by the pick is stored in the rock as elastic energy until the crack is initiated according to the linear elastic fracture mechanics Griffith and Eng (1921). The work done by the pick is:

$$\begin{aligned} U_0 &= \int \Delta U dA = \int_0^d \int_{-\pi/2}^{\pi/2} \frac{\sigma^2}{2E} r d\theta \frac{dl}{\cos(\beta)} \\ &= \int_0^d \int_{-\pi/2}^{\pi/2} \left[\frac{2}{\pi} \left(\frac{\sin(\alpha)}{\cos(\beta)} - 1 \right) \theta + 1 \right] \frac{(d-l)^2 K_{Ic}^2}{2\pi d^2 E \delta_{li} \cos(\beta)} \lambda l d\theta dl \\ &= \frac{\lambda_{li} K_{Ic} d^2}{24 E \delta_{li} \cos(\beta)} \left[\frac{1}{3} \left(\frac{\sin(\alpha)}{\cos(\beta)} - 1 \right)^2 + 1 \right] \end{aligned} \tag{A.18}$$

Combining Equations A.16, A.17 and A.18, the size of the crack when it is initiated becomes:

$$\delta_{li} = \sqrt[3]{\frac{\lambda_{li} d^2}{12\pi \cos(\beta)} \left[\frac{1}{3} \left(\frac{\sin(\alpha)}{\cos(\beta)} - 1 \right)^2 + 1 \right]} \tag{A.19}$$

Finally, the peak cutting force is calculated by combining Equation A.15 with A.19 which leads to:

$$PCF_{Li} = \frac{\lambda_{li}^{\frac{5}{6}} K_{Ic} d^{\frac{5}{3}}}{3 \sqrt[6]{\frac{\pi^2}{12\cos(\beta)} \left[\frac{1}{3} \left(\frac{\sin(\alpha)}{\cos(\beta)} - 1 \right)^2 + 1 \right]}} \tag{A.20}$$

B | Appendix B

B.1 Experimental dataset from Copur et al. (2003).

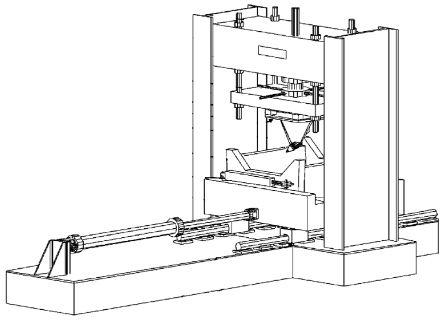

Figure B.1: Schematic drawing of linear cutting experiment machine Tuncdemir et al. (2008).

Table B.1: Experimental results linear unrelieved cutting test from Copur et al. (2003).

Rock type	UCS	BTS	Cutting Depth	MCF	MNF	PCF	PNF	Mean Specific Energy
	$[MPa]$	$[MPa]$	$[mm]$	[kN]	[kN]	[kN]	[kN]	[kWh/m^3]
Harsburgite	58	5.5	5	5.21	6.09	14.69	14.20	18.6
			9	9.04	9.34	26.40	21.46	9.4
Serpantinite	38	5.7	5	2.89	3.20	7.70	8.66	9.5
			9	6.97	8.07	19.77	17.27	8.1
Trona	30	2.2	5	1.36	2.11	3.81	4.81	8.7
			9	4.12	6.27	12.03	13.54	6.7
Limestone	121	7.8	3	3.87	7.49	11.62	14.99	31.7
			5	7.32	12.30	21.10	26.76	19.2
			9	11.94	20.02	32.23	38.18	16.4
Claystone	58	5.6	3	1.17	1.12	3.75	3.29	13.0
			5	2.95	2.91	8.80	8.04	14.1
			7	3.17	2.75	10.78	8.75	7.9
			9	5.25	3.83	16.60	10.86	6.6
Sandstone-1	114	6.6	3	3.84	4.33	8.96	8.61	47.2
			5	7.44	7.71	19.32	15.74	23.4
			9	9.73	8.52	28.96	21.47	13.5
Sandstone-2	174	11.6	3	4.02	5.97	9.03	11.08	54.3
			5	8.04	10.63	22.81	23.41	49.6
			9	16.54	18.92	47.19	42.04	21.4
Siltstone	58	5.3	3	3.07	4.34	7.34	10.21	42.1
			5	7.27	9.41	22.60	22.49	24.0
			9	8.27	8.47	31.39	23.64	15.5
High grade chromite	32	3.7	5	2.74	2.27	7.02	5.42	11.1
			9	5.20	3.47	14.55	9.05	5.8
Medium grade chromite	47	4.5	5	3.40	2.96	10.02	7.71	14.8
			9	9.13	6.53	25.99	16.18	12.0
Low grade chromite	46	3.7	5	3.13	2.80	8.54	7.00	11.7
			9	6.50	5.61	15.93	11.62	11.0

B.2 Comparison of rock cutting models with experiments.

Table B.2: Comparison of the linear rock cutting models with the mean cutting forces obtained from the experiments of Copur et al. (2003)

Rock type	UCS [MPa]	BTS [MPa]	Cutting Depth [mm]	MCF Experiment [kN]	MCF Li [kN]	MCF Bilgin [kN]
Harsburgite	58	5.5	5	5.21	3.43	3.42
			9	9.04	9.13	6.15
Serpantinite	38	5.7	5	2.89	2.90	2.61
			9	6.97	7.73	4.69
Trona	30	2.2	5	1.36	1.74	2.28
			9	4.12	4.64	4.11
Limestone	121	7.8	3	3.87	2.33	3.58
			5	7.32	5.46	5.97
			9	11.94	14.55	10.75
Claystone	58	5.6	3	1.17	1.47	2.05
			5	2.95	3.45	3.42
			7	3.17	6.05	4.78
			9	5.25	9.20	6.15
Sandstone-1	114	6.6	3	3.84	2.12	3.41
			5	7.44	4.96	5.69
			9	9.73	13.20	10.23
Sandstone-2	174	11.6	3	4.02	3.23	4.87
			5	8.04	7.58	8.12
			9	16.54	20.18	14.61
Siltstone	58	5.3	3	3.07	1.44	2.05
			5	7.27	3.37	3.42
			9	8.27	8.98	6.15
High grade chromite	32	3.7	5	2.74	2.24	2.36
			9	5.20	5.96	4.25
Medium grade chromite	47	4.5	5	3.40	2.87	2.97
			9	9.13	7.65	5.35
Low grade chromite	46	3.7	5	3.13	2.62	2.93
			9	6.50	6.97	1.92

Table B.3: Comparison of the linear rock cutting models with the peak cutting forces obtained from the experiments of Copur et al. (2003)

Rock type	UCS	BTS	Cutting Depth	PCF Experiment	PCF Nishimatsu	PCF Miedema	PCF Evans 2D	PCF Evans 3D	PCF Goktan	PCF Goktan 2005	PCF Li
	[MPa]	[MPa]	[mm]	[kN]	[kN]	[kN]	[kN]	[kN]	[kN]	[kN]	[kN]
Harsburgite	58	5.5	5	14.69	0.24	0.63	1.62	1.12	1.58	6.86	7.71
			9	26.40	0.78	2.03	5.24	3.62	5.11	22.23	20.54
Serpantinite	38	5.7	5	7.70	0.16	0.65	1.67	1.12	1.63	7.11	6.53
			9	19.77	0.51	2.10	5.43	5.93	5.30	23.04	17.39
Trona	30	2.2	5	3.81	0.13	0.25	0.65	1.83	0.63	2.74	3.92
			9	12.03	0.41	0.81	2.09	1.12	2.04	8.89	10.43
Limestone	121	7.8	3	11.62	0.18	0.32	0.83	0.39	0.81	3.50	5.25
			5	21.10	0.50	0.89	2.29	1.08	2.24	9.73	12.29
			9	32.23	1.63	2.88	7.43	3.49	7.25	31.53	32.75
Claystone	58	5.6	3	3.75	0.09	0.23	0.59	0.42	0.58	2.52	3.32
			5	8.80	0.24	0.64	1.65	1.16	1.61	6.99	7.77
			7	10.78	0.47	1.25	3.23	2.27	3.15	13.69	13.62
			9	16.60	0.78	2.07	5.33	3.75	5.20	22.64	20.70
Sandstone-1	114	6.6	3	8.96	0.17	0.27	0.70	0.29	0.68	2.52	4.76
			5	19.32	0.48	0.75	1.94	0.82	1.89	8.23	11.15
			9	28.96	1.54	2.44	6.28	2.65	6.13	26.68	29.71
Sandstone-2	174	11.6	3	9.03	0.26	0.48	1.23	0.60	1.20	2.96	7.28
			5	22.81	0.73	1.32	3.41	1.66	3.33	14.47	17.05
			9	47.19	2.35	4.28	11.04	5.37	10.78	46.89	45.41
Siltstone	58	5.3	3	7.34	0.09	0.22	0.56	0.37	0.55	2.38	3.24
			5	22.60	0.24	0.60	1.56	1.04	1.52	6.61	7.59
			9	31.39	0.78	1.96	5.05	3.36	4.93	21.43	20.22
High grade chromite	32	3.7	5	7.02	0.13	0.42	1.09	0.92	1.06	4.62	5.04
			9	14.55	0.43	1.37	3.52	2.97	3.44	14.96	13.41
Medium grade chromite	47	4.5	5	10.02	0.20	0.51	1.32	0.92	1.29	5.61	6.46
			9	25.99	0.63	1.66	4.28	2.99	4.18	18.19	17.21
Low grade chromite	46	3.7	5	8.54	0.19	0.42	1.09	0.92	1.06	4.62	5.89
			9	15.93	0.62	1.37	3.52	2.06	3.44	14.96	15.68

C | Appendix C

Calculation procedure according to Schulte (2013)

The momentum balance calculates the liquid flux j_L and solid flux j_S for a given gas flux $j_{G.atm}$. The procedure to calculate the solid flux j_S and liquid flux j_L for a known value of $j_{G.atm}$ is shown in Figure C.1 and divided into 7 steps:

1. Determine the basic variables to use in the rest of the calculation.
2. Use the bisection method to find the solid flux value of j_L and associated value of j_S.
3. Start the iteration of the pressure over depth. As a first estimate, use a the water pressure at the depth of the air inlet (I) for calculating the pressure with Equations C.1 and C.2.
4. Calculate the solid and liquid concentrations C_{S2}, C_{S3}, C_{L2}, C_{L3} with Equation C.3 till C.10.
5. Calculate the gas concentration C_g with Equations C.11 till C.13. Reiterate this step with step 4 until the difference in concentration is smaller than 10^-5.
6. Calculate the pressure losses over the pipe for the two phase flow and for the three-phase flow with Equations C.14 till C.20. Incorporate the pressures losses in the pressure profile along the vertical, which results in a non-linear behaviour of the pressure. Repeat this 10 times with step 3 and 4.
7. Calculate the momentum balance with Equation C.21. As long as the absolute value of the equation is above 100, use the bisection method to repeat step 3 till 6 to find a value for the momentum balance that is below 100.

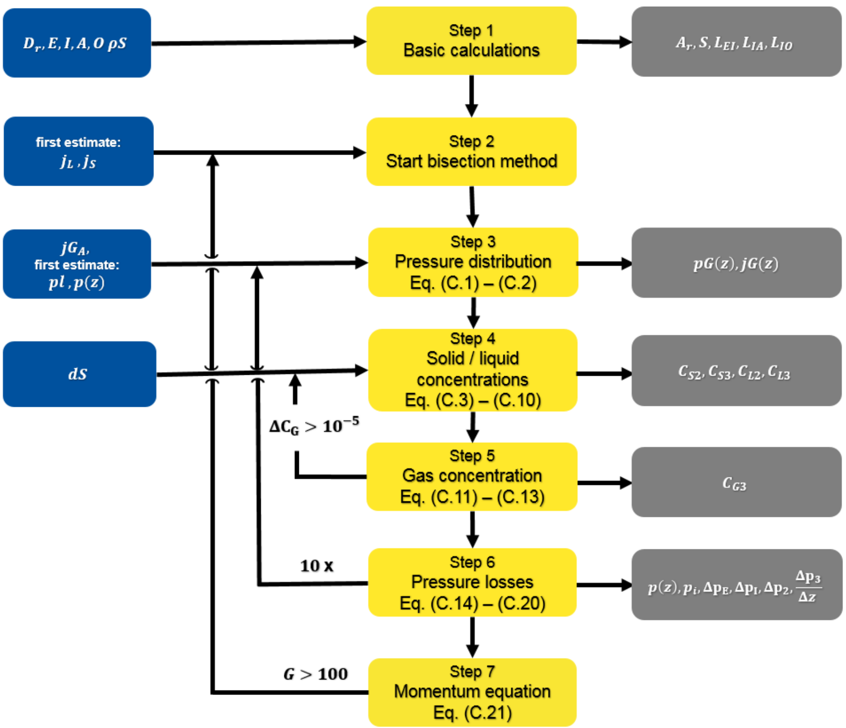

Figure C.1: Calculation procedure based on Schulte (2013).

Pressure distribution
Both the gas flux and density vary over depth and are calculated with:

$$\rho_G(z) = \frac{p(z)}{RK} \tag{C.1}$$

$$j_G(z) = j_{G.atm}\frac{p_{atm}}{p(z)} \tag{C.2}$$

Where ρ_G is the density of the gas, j_G is the flux of the gas, $j, G.atm$ equals the flux at atmospheric pressure, R is the gas-constant and T the temperature in Kelvin.

Solid and liquid concentration

In order to calculate the solid and liquid concentrations, the hindered settling theory described by Rhee (2018) is used. The relation between the relative velocities and the concentrations is given by:

$$w_S = v_L - v_S = \frac{j_L}{C_L} - \frac{j_S}{C_S} \tag{C.3}$$

Where w_S is the hindered settling velocity of the particles, v_L is the velocity of the liquid, v_S the velocity of the solids, j_L the liquid flux, j_S the solid flux and C_L and C_S the liquid and solids concentrations.

Assumed is that all the particles are suspended in the liquid, therefore the concentration of the combined concentration can be described by:

$$C_{LS} = C_S + C_L = 1 - C_G \tag{C.4}$$

Filling Equation C.4 into Equation C.3 leads to the following equation for the three phase part:

$$C_L^2 + (\frac{-C_{LS}w_S - j_L - j_S}{v_r})C_L + \frac{C_{LS}j_L}{w_s} \tag{C.5}$$

In the two phase part there is no concentration of gas, which simplifies the equation towards:

$$C_L^2 + \frac{-w_S - j_L - j_S}{w_S} \cdot CL + \frac{j_L}{v_r} = 0 \tag{C.6}$$

From where the liquid and respectively the solid concentration can be solved with the ABC formula if the relative velocities between the solids and the liquid are known. According to the theory described by Rhee (2018), the formula relative velocity between the particles and the liquid according to the hindered settling theory equals:

$$w_S = \zeta_f(1 - \frac{C_S}{1 - C_G})^{n_h}w_0 \tag{C.7}$$

Where ζ_f is defined as a form factor, n_h is the hindered settling particle factor and w_0 is the settling velocity of a single particle which can be calculated with:

$$w_0 = \sqrt{\frac{4(\rho_S - \rho_L)gd_S}{3\rho_L C_D}} \tag{C.8}$$

Where ρ_S is the particle density, ρ_L is the water density, g is the gravity constant, d_S is the particle diameter and C_D is the drag coefficient, which is assumed to be 0.42.

n_h depends on the particle Reynolds number Re_p which is defined by:

$$n_h = \frac{4.7 + 0.41Re_p^{0.75}}{1 + 0.175Re_p^{0.75}} \tag{C.9}$$

The particle Reynolds can be calculated with:

$$Re_p = \frac{w_S d_S}{\nu} \tag{C.10}$$

Where d_S is the density of the particles and ν is the kinematic viscosity of water. The particle Reynolds number is depends on the hindered settling velocity w_S and therefore requires iteration. To define the number, use the settling velocity of a single particle as a first approximation. Thereafter, the hindered settling velocity is used till a stable value of w_S is reached.

Gas concentration

The concentration of gas C_G depends on the slip ratio between the gas and the mixture of the solids and the liquid and is calculated according to Schulte (2013) with:

$$C_G = \frac{1}{1 + 0.4\frac{\rho_G}{\rho_{LS.3}}(\frac{1}{\alpha_x} - 1) + 0.6\frac{\rho_G}{\rho_{LS.3}}(\frac{1}{\alpha_x} - 1)\sqrt{\frac{\frac{\rho_{LS.3}}{\rho_G} + 0.4(\frac{1}{\alpha_x} - 1)}{1 + 0.4(\frac{1}{\alpha_x} - 1)}}} \tag{C.11}$$

Where α_x is the ratio of the mass flux of air compared to the entire mass flux of the mixture defined by:

$$\alpha_x = \frac{\rho_G j_G}{\rho_G j_G + \rho_L j_L \rho_S j_S} \tag{C.12}$$

and $\rho_{LS.3}$ is the density of the combined solid and liquid flow and is calculated with:

$$\rho_{LS.3} = \rho_L \cdot \frac{C_L}{1 - C_G} + \rho_S \cdot \frac{C_S}{1 - C_G} \tag{C.13}$$

Pressure losses

The pressure losses can be divided in two-phase losses and three-phase losses. The losses in the two-phase part are due to entrance loss Δp_E and friction loss Δp_2 and can be calculated with:

$$\Delta p_E = (\xi_E + \xi_a)\frac{1}{2}q_2 \tag{C.14}$$

$$\Delta p_2 = \lambda \frac{L_{EI}}{D}\frac{1}{2}q_2 \tag{C.15}$$

Where ξ_E and ξ_a are respectively the friction coefficients ($\xi_E = 0.56$ and $\xi_a = 1$) due to inlet losses which are defined by Yoshinaga and Sato (1996), λ is the Darcy friction factor is calculated according to Nikuradse (1950), assuming Re $>$ 100.000:

$$\lambda = \frac{0.25}{\left(log\left(3.7\frac{D_{tube}}{k1000}\right)\right)^2} \tag{C.16}$$

q_2 is the dynamic pressure loss, which can be calculated with:

$$q_2 = C_{L.2}\rho_L v_L^2 + C_{S.2}\rho_s v_s^2 \tag{C.17}$$

In the three phase part the losses can be divided into an acceleration loss in the gas inlet and friction losses:

$$\Delta p_I = \xi_a \cdot \frac{1}{2} \cdot (q_3(1) - q2) \tag{C.18}$$

$$\frac{\Delta p_3}{\Delta z} = \lambda \frac{1}{D}\frac{1}{2}q_3 \tag{C.19}$$

Where D is the diameter of the pipe, ξ_a is the friction coefficient due to acceleration loss and q_3 is the dynamic pressure loss according to:

$$q_3(z) = C_G(z) \cdot \rho_G(z) \cdot v_G(z)^z + C_{L.3}(z) \cdot \rho_L \cdot v_L(z)^2 + C_{S.3}(z) \cdot \rho_s \cdot v_s(z)^2 \tag{C.20}$$

Momentum equation

$$\begin{aligned} &\underbrace{A_r\{j_l\rho_l v_{l,E} + j_s\rho_s v_{s,E}\}}_{G_1} - \underbrace{A_r\{j_{g,O}\rho_{g,O}v_{g,O} + j_l\rho_l v_{l,O} + j_s\rho_s v_{s,O}\}}_{G_2} \\ &+ \underbrace{A_r\{\Delta p_2 + \Delta p_E\}}_{G_3} + \underbrace{A_r\{\int_I^O p_3(z)dz + \Delta p_I\}}_{G_4} - \underbrace{A_r g L_{EI}\{\rho_L C_{L,2} + \rho_s C_{S,2}\}}_{G_5} \\ &\underbrace{- A_r g \int_I^O \{\rho_G(z)C_G(z) + \rho_L C_{L,3}(z) + \rho_S C_{S,3}(z)\}dz}_{G_6} + \underbrace{A_r\{\rho_L g(L_{EI} + L_{IA})\}}_{G_7} = 0 \end{aligned} \tag{C.21}$$

D | Appendix D

D.1 Simulation data Kure Copper Mine

Table D.1: Input parameters simulation Kure Copper Mine obtained from Shaterpour-Mamaghani and Bilgin (2016).

Parameter	**Value**	**Unit**
Diameter	2.6	m
Thrust	4160	kN
Torque	173	kNm
Break out torque	210	kNm
Pilot rotational speed	$0-52$	rpm
Reaming rotational speed	$0-17$	rpm
Power	$200-250$	kW
Derreck weight	13150	kg
Number of roller bits	16	-
Number of indenters per bit	129	-
Dimensions indenter	17 x 8	mm
Unconfined Compressive Strength	81.6 ± 29.3	MPa
Brazilian Tensile Strength	10.96 ± 2.7	MPa
Density	2810	kg/m^3

Table D.2: Comparison between excavation model and data from Shaterpour-Mamaghani and Bilgin (2016).

Rod nr. [-]	**Operating Thrust** [kN]	**Operating Torque** [kNm]	**Rotational speed** [rpm]	**ROP** [m/h]	**ROP (model)** [m/h]
15	176	37	4	0.96	0.062
14	757	54	6	0.764	0.428
13	988	63	7	0.876	0.584
12	608	66	7	1.135	0.617
11	1221	86	9	0.985	1.048
10	1270	85	9	1.409	1.037
9	1245	91	9	1.233	1.118
8	1349	93	8	1.054	1.018
7	1382	94	10	1.433	1.284
6	1498	94	10	1.146	1.284
5	1472	96	10	1.178	1.314
4	1493	94	9	1.141	1.156
3	1436	94	9	1.159	1.156
2	1323	84	9	0.888	1.026
1	1444	98	9	1.184	1.210
Pilot hole	354	38	7	3.41	0.344

D.2 Simulation data Olkiluoto

Table D.3: Input parameters Olkiluoto obtained from Autio and Kirkkomäki (1996).

Parameter	Value	Unit
Diameter	1.5	m
Thrust	630	kN
Torque	74	kNm
Reaming rotational speed	$0-12$	rpm
Number of roller bits	8	-
Number of rows per bit	$4-6$	-
Dimensions indenters	5 - 15	mm

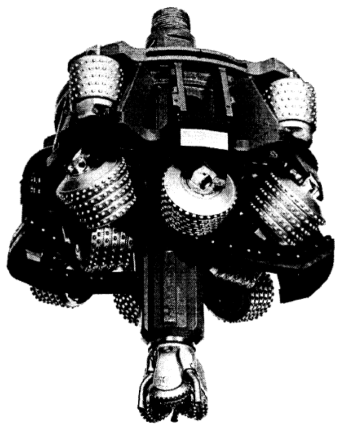

Figure D.1: Reamer head used in the research Tunnel at Olkiluoto Autio and Kirkkomäki (1996).

Table D.4: Comparison between excavation model and data from Autio and Kirkkomäki (1996) for boring the second hole with 5-6 rows per bit.

Test	Operating Thrust [kN]	Operating Torque [kNm]	Rotational speed [rpm]	ROP [m/h]	ROP (model) [m/h]
2.4.1	718.5	29.2	8.1	0.76	0.89
2.4.2	608.8	28.9	8.1	0.7	0.78
2.4.3	497.2	23.6	8.4	0.51	0.68
2.4.4	492.9	24.3	8.6	0.55	0.69
2.4.5	401.0	21.5	8.9	0.39	0.60
2.4.6	401.0	21.1	8.9	0.39	0.60
2.6.1	730.7	37.0	8.1	1.03	0.90
2.6.2	503.9	25.0	8.1	0.49	0.67
2.6.3	407.7	21.1	8.3	0.39	0.57
2.6.4	311.5	18.7	7.6	0.26	0.42
2.7.1	723.0	35.9	7.7	0.88	0.85
2.7.2	668.0	31.7	8.3	0.82	0.86
2.7.3	547.0	26.4	8.3	0.63	0.73
2.7.4	423.3	22.5	8.4	0.44	0.60

Table D.5: Comparison between excavation model and data from Autio and Kirkkomäki (1996) for boring the third hole with 4-5 rows per bit.

Test	**Operating Thrust** [kN]	**Operating Torque** [kNm]	**Rotational speed** [rpm]	**ROP** [m/h]	**ROP (model)** [m/h]
3.8.1	412.0	20.4	8.4	0.31	0.44
3.8.2	497.2	22.5	8.3	0.41	0.52
3.8.3	597.8	25.7	8.1	0.51	0.60
3.8.4	307.0	18.0	8.4	0.2	0.33
3.8.5	409.8	20.4	8.4	0.35	0.44
3.8.6	497.2	22.5	8.3	0.45	0.52
3.8.7	356.1	20.4	8.7	0.30	0.40
3.11.1	606.7	28.5	8.1	0.69	0.61
3.11.2	307.1	19.4	8.4	0.30	0.34
3.11.3	407.7	21.8	8.3	0.41	0.43
3.11.4	506.1	25.7	8.3	0.53	0.53
3.12.1	728.5	31.7	8.0	0.78	0.69
3.12.2	607.8	28.9	8.0	0.67	0.60
3.12.3	507.3	24.7	8.0	0.53	0.51
3.12.4	413.2	22.9	8.4	0.42	0.44
3.12.5	312.7	19.4	8.6	0.27	0.35
3.12.6	737.4	34.2	8.1	0.81	0.71

Table D.6: Comparison between excavation model and data from Autio and Kirkkomäki (1996) for different rotational speeds.

Test	**Operating Thrust** [kN]	**Operating Torque** [kNm]	**Rotational speed** [rpm]	**ROP** [m/h]	**ROP (model)** [m/h]
2.5.1	724.6	32.8	4.1	0.47	0.35
2.5.2	724.6	33.8	7.7	0.8	0.65
2.5.3	694.4	37.3	11.8	1.02	0.95
3.9.1	603.3	28.5	9.6	0.87	0.71
3.9.2	596.8	28.9	11.8	0.90	0.86
3.9.3	596.8	25.4	4.4	0.37	0.32
3.10.1	730.7	34.2	7.6	1.09	0.66
3.10.2	725.2	33.1	6.4	0.79	0.55
3.10.3	722.4	37.0	11.8	1.23	1.01

D.3 Weber

Table D.7: Simulation data from Weber and Dedegil (1976) compared with the results of the transport model.

Nr	Density	d_s	L_{EI}	L_{IA}	L_{AO}	Q_g	Q_l	Q_s	Q_s (model)
-	[kg/m^3]	[mm]	[m]	[m]	[m]	[m^3/h]	[m^3/h]	[m^3/h]	[m^3/h]
Gravel									
1	2575	5	101	171	7.0	673.2	637.2	7.3	13.5
2	2575	5	101	174	7.0	921.6	687.6	16.1	19.7
3	2575	5	101	177	7.0	1382.4	583.2	20.5	39.8
4	2575	5	101	180	7.0	1458.0	835.2	34.3	25.9
5	2575	5	101	186	7.0	936.0	702.0	13.6	19.2
6	2575	5	101	216	7.0	896.4	630.0	13.9	21.2
7	2575	5	101	218	6.9	1429.2	709.2	29.9	33.6
8	2575	5	101	222	6.9	1184.4	723.6	27.8	25.4
9	2575	5	101	225	6.9	864.0	576.0	14.8	22.5
10	2575	5	290	69	6.6	2052.0	687.6	14.5	13.7
11	2575	5	290	111	6.6	1346.4	446.4	20.0	19.7
12	2575	5	290	152	7.7	943.2	608.4	9.3	10.8
13	2575	5	341	104	6.3	1958.4	568.8	19.0	20.5
14	2575	5	197	246	6.8	1836.0	720.0	33.6	31.1
15	2575	5	197	246	7.3	1321.2	738.0	19.5	18.7
16	2575	5	6.2	42	7.2	2070.0	918.0	45.7	49.5
17	2575	5	6.2	42	7.2	1404.0	892.8	24.5	26.9
18	2575	5	6.2	42	7.2	838.8	694.8	19.2	24.7
Sand									
19	2610	0.5	197	245	7.4	1742.4	671.4	27.0	32.1
20	2610	0.5	4.9	246	6.4	907.2	732.6	19.9	26.9
21	2610	0.5	4.9	248	8.4	1404.0	597.6	45.8	53.7
22	2610	0.5	4.9	248	8.4	1641.6	640.1	43.7	60.4
23	2610	0.5	101	248	8.4	1756.8	618.5	38.7	45.8
24	2610	0.5	101	148	8.9	792.0	554.4	18.6	20.0
25	2610	0.5	101	148	8.4	1278.0	634.7	40.6	32.9